RSC Advances

ROYAL SOCIETY OF CHEMISTRY

PAPER

View Article Online
View Journal | View Issue

Cite this: *RSC Adv.*, 2026, **16**, 19158

Fabrication of Co_3O_4/P-rGO for electrocatalytic reduction of greenhouse CO_2 gas into value-added chemicals in aqueous solution

Rad Mosharrof Mim,[a] Md. Shamim Alam,[b] Sangjukta Yesmin,[a] Md. Mominul Islam,[c] Chanchal Kumar Roy,[a] Abu Bin Imran *[a] and Al-Nakib Chowdhury*[a]

The electrocatalytic reduction of greenhouse CO_2 gas into value-added fuels or chemical feedstocks sustainably addresses energy and environmental crises. However, CO_2 reduction is particularly effective with electrocatalysts, which exhibit distinct functionality at electrode surfaces. In this work, we demonstrate the electrocatalytic reduction of CO_2 using flower-like cobalt oxide (Co_3O_4) synthesized *via* a hydrothermal method. Co_3O_4 is incorporated into P-doped rGO *via* ultrasonication to form a hybrid electrocatalyst, thereby enhancing CO_2 reduction efficiency by improving electrode surface functionality. Chemical, morphological, and structural characterization of the synthesized catalyst was carried out using scanning electron microscopy (SEM), X-ray diffraction (XRD), Raman spectroscopy, and X-ray photoelectron spectroscopy (XPS) analysis. The electrocatalytic reduction of CO_2 was performed in 0.5 M $NaHCO_3$ aqueous solution at a pH of 7.5 (CO_2 conditions) in a three-electrode system and applying potential *vs.* Ag/AgCl (3 M KCl sat.) as the reference electrode, platinum wire as the counter electrode, and the prepared catalyst as a modified graphite working electrode. Chronoamperometry shows CO_2 conversion stability under a constant voltage of −0.62 V (*vs.* Ag/AgCl) for 2.5 hours. The Co_3O_4 catalyst primarily yields ethanoic acid with 69% faradaic efficiency at a current density of −0.5 mA cm^{-2}. Additionally, ethanoic acid and propanal are detected for the hybrid flower-like Co_3O_4/P-rGO catalyst, with 58% and 9% faradaic efficiencies at a constant current density of −0.8 mA cm^{-2}. These results highlight that incorporating Co_3O_4 into the P-rGO improves reduction performance. This can provide a promising platform for synthesizing and fabricating shape-based materials as an electrocatalyst, paving the way for a future powered by renewable, boundless energy and wealth from greenhouse CO_2 gas and other pollutants.

Received 22nd February 2026
Accepted 7th April 2026

DOI: 10.1039/d6ra01555g

rsc.li/rsc-advances

1. Introduction

The increasing atmospheric CO_2 is a harmful greenhouse gas and the main contributor to global warming.[1] Global warming leads to a series of problems, such as environmental pollution, ozone layer depletion, extreme weather, and desertification.[2] Conversely, nature maintains a delicate balance in the carbon cycle by regulating the consumption and emission of CO_2 from various sources. Anthropogenic activities, particularly fossil fuel combustion and industrial processes, emit approximately 37.4 Gt of CO_2 per year, accounting for about 65% of total greenhouse gas emissions, and this cannot be accommodated in the natural carbon cycle.[3] To keep humanity safe and secure, mitigating the challenge of increasing CO_2 is now becoming a global concern. In managing this, converting CO_2 into value-added chemicals or fuels appears to be the most attractive to scientists and technologists.[4]

In this regard, the conversion of captured CO_2 *via* chemical, photochemical, electrochemical, and biochemical processes appears to be extremely prevalent in modern technology.[5] Compared to other conversion techniques such as thermal and photochemical processes, electrocatalytic reduction of CO_2 is a simple, eco-friendly, and cost-effective approach that provides high-value reduction products with high conversion stability.[6,7] A much higher negative potential of −1.9 V is needed for the electrochemical reduction of CO_2.[8] This potential may increase due to the overpotential and kinetic barrier of the electrode used in the electrochemical approach for CO_2 reduction. To resolve these problems, a strong electrocatalyst is highly needed, combining high faradaic efficiency and good conversion stability with reduced reaction overpotential for the electrochemical reduction of CO_2. Several catalysts, such as bimetallic compounds[9,10] metal oxide derivatives[10,11] and metal–

[a]*Department of Chemistry, Bangladesh University of Engineering and Technology, Dhaka-1000, Bangladesh. E-mail: abimran@chem.buet.ac.bd; nakib@chem.buet.ac.bd*

[b]*Department of Textile Engineering, Southeast University, Tejgaon I/A, Dhaka, Bangladesh*

[c]*Department of Chemistry, University of Dhaka, Dhaka-1000, Bangladesh*

organic hybrid materials[12,13] have already been used for the electrocatalytic reduction of CO_2. Among these, metal oxide-based catalysts are very efficient due to their high product selectivity, high conversion efficiencies, and low overpotential for the reduction of CO_2 compared to pure metallic forms. Various metal oxide-based catalysts, such as CuO,[14] Cu_2O,[15] Sn_3O_4,[16] SnO_2,[17] NiO,[18] Pb_3O_4,[19] Co_3O_4,[20] MnO_2,[21] Fe_3O_4 (ref. 22) are used for the electrochemical reduction of CO_2. Due to low cost, most abundant and high catalytic activity, a shape-controlled Co_3O_4 is promising for CO_2 conversion yielding methanol, formic acid, and ethanol as the value-added chemicals.[23] Co_3O_4 is well suited for heterogeneous catalysis because of its redox reactivity. The dual oxidation state[24] Co^{2+}/Co^{3+} can provide thermodynamic stability to the Co_3O_4 catalyst.[25,26] With that, the d orbitals of Co ions grant more active sites for conducting various reactions to function as an oxidizing or reducing character at ambient conditions.[24] Various morphology-based Co_3O_4, such as nanofibrous,[27] crystal facet-tailored,[28] self-templated hierarchical nanosheets,[29] hollow multi-shelled structured,[30] nano-cube[31] like Co_3O_4 have already been used as an electrocatalyst for the electrochemical reduction of CO_2. It is quite certain that Co_3O_4 can play a strong role as an electrocatalyst, but the Co ion suffers agglomeration problems in electrolyte solutions, and it creates low conductivity, which can reduce the transportation of electrons and its active sites during the reaction time.[32,33]

Thus, if a support of another conductive material, such as graphene oxide (GO),[34] reduced graphene oxide (rGO),[35] polyaniline,[36] g-C_3N_4,[37] is incorporated into a metal substrate, then the reduction might be more effective. Among the supports, rGO is the most attractive in CO_2 conversion due to its high surface area, intrinsic mobility, excellent mechanical strength, and thermal conductivity.[38] The large surface area of rGO enhances CO_2 adsorption on the electrode surface. The adsorption of CO_2 on the electrode surface can tune the conversion efficiencies or the faradaic efficiencies of selective products.[39] On the other hand, doping rGO with foreign materials like nitrogen (N), phosphorus (P), and sulphur (S) can modulate the electronic aspects of the rGO and thus make it more conductive than its undoped state. Heteroatoms with different electronegativity N (3), S (2.5), P (2.1) can break the electroneutrality of graphene derivatives, and show a tremendous role as a supporting material for the different electrochemical applications, including water splitting, batteries, supercapacitors, and fuel cells.[40,41] P is an efficient dopant for its electronic stability with changeable electronic valences. It also has lower electronegativity from carbon and high electron-donating ability, which can modulate the carbon atom's electronic surrounding and local charge density in rGO materials.[42] Incorporation of P into graphene derivatives can induce more active sites due to the larger size and lower electronegativity of P than any other dopant. Not only the active sites, but also the lone pair of P can provide a conjugation with the graphene π system, and that can also modulate the band structure, electrical and chemical reactivity of graphene derivatives.[43,44] The conjugation between dopant and substrate might be particularly worthy cause the impact of any heteroatom doping of graphene significantly depends on the nature of bonding involved. G. Bharath *et al.* have shown that using self-assembled Co_3O_4 nanospheres on N-doped reduced graphene oxide (Co_3O_4/N-rGO) bifunctional catalyst has shown an excellent application for CO_2 reduction, yielding methanol with 74.8% faradaic efficiency.[45] Hence, it is expected that, when rGO support is doped with P and incorporated into the flower-like Co_3O_4, it would be able to yield a potential hybrid catalyst. In that case, the hybrid should perform more than the single entity present in the hybrid catalyst.

This study introduces a novel approach of morphology-based work for the electrochemical reduction of CO_2, which has not previously been reported. In this regard, the flower-like Co_3O_4 and flower-like Co_3O_4/P-rGO hybrid catalyst will be synthesized using hydrothermal and ultrasonication methods, respectively, and evaluated as a cathode for the electrochemical reduction of greenhouse CO_2 gas. Various analytical methods, including XRD, FESEM, EDX, Raman, and XPS, are used to assess the chemical and morphological aspects of the catalyst. Therefore, catalytic stability, product selectivity, and faradaic efficiency of produced value-added chemicals or fuels will be analyzed to comprehensively evaluate the performance of the electrocatalytic reduction of CO_2 gas, providing insights into their potential for sustainable CO_2 conversion to useful chemicals and fuels.

2. Materials and methods

2.1 Materials

Sodium nitrate ($NaNO_3$), hexamethylenetetramine ($C_6H_{12}N_4$), cobalt nitrate hexahydrate ($Co(NO_3)_2 \cdot 6H_2O$), absolute ethanol (C_2H_5OH) (G.R. 99.7%), graphite powder, nitric acid (HNO_3), sulfuric acid (H_2SO_4), potassium permanganate ($KMnO_4$), hydrogen peroxide (H_2O_2), di-potassium hydrogen phosphate (K_2HPO_4), deionized water, sodium bicarbonate ($NaHCO_3$), Nafion-117, dimethylsulfoxide (DMSO, A.R., 99.5%) were purchased from Sigma-Aldrich, India. All chemicals were used without further purification. The CO_2 and N_2 (purity: 99.99%) gases were purchased from Essence Industrial Gas Limited, Dhaka, Bangladesh.

2.2 Synthesis of Co_3O_4

A facile low-temperature hydrothermal process is used to synthesize flower-like Co_3O_4. The molar ratio of precursors ($NaNO_3$, HMTA, $Co(NO_3)_2 \cdot 6H_2O$) was maintained at 1 : 1 : 0.2. 0.85 g of $NaNO_3$ and 1.7776 g of HMTA were dissolved in a mixture of 40 mL of deionized water and 5 mL of anhydrous ethanol, followed by the addition of 0.58 g of Co $(NO_3)_2 \cdot 6H_2O$. The obtained light pink colored homogeneous solution was then transferred into a 100 mL Teflon-lined stainless autoclave for hydrothermal treatment at 110 °C for 3 h. Subsequently, the autoclave cooled to ambient temperature, and the resultant green precipitate was collected by centrifugation and washed three times with water and anhydrous ethanol. The green residue was dried at 70 °C for 10 h. Finally, the dried green

powder of cobalt was calcined at 400 °C for 2 h in ambient atmosphere, and the black Co_3O_4 samples were obtained.

2.3 Synthesis of P-doped rGO

GO is synthesized by harsh oxidation of the graphite powders by modified Hummers' method.[46] Then, the P-doped rGO is synthesized by a conventional one-step hydrothermal method. 200 mg GO was dispersed in 60 mL deionized water by sonicating in an ultrasonic bath at 10 kHz frequency until a homogeneous mixture was obtained. To this dispersion, 1 g, 2 g, and 4 g of di-potassium hydrogen phosphate were added separately to the GO suspension and further sonicated for 2 h. Each resulting suspension was transferred to the 100 mL Teflon-lined stainless autoclave for hydrothermal treatment at 180 °C for 12 h. Subsequently, the autoclave cooled to ambient temperature, and the resultant black precipitate was filtered and washed with deionized water and ethanol several times. Finally, the resultant black precipitates of P-doped rGO (P-rGO) were dried at 60 °C for 12 h in a vacuum oven. Here, the obtained samples were labeled as $P_{(0.5\%)}$rGO, $P_{(1\%)}$rGO, and $P_{(2\%)}$rGO corresponding to the increase of P content.

2.4 Synthesis of shape controlled Co_3O_4/P doped rGO

30 mg of P-rGO with varying P content $P_{(0.5\%)}$rGO, $P_{(1\%)}$rGO and $P_{(2\%)}$rGO was mixed separately to 90 mg of Co_3O_4 in 120 mL ethanol. The resultant mixture was ultrasonicated at 10 kHz frequency for 5 h. Initially, the suspension was sonicated for 2.5 h at room temperature and then at 60 °C. The suspension was then dried at 70 °C in a vacuum oven. The powder was washed with deionized water three times and further dried at 70 °C for 12 h in a vacuum oven. As a result, Co_3O_4/P-rGO hybrid composite with different phosphorus contents was successfully obtained and designated as $Co_3O_4/P_{(0.5\%)}$rGO, $Co_3O_4/P_{(1\%)}$rGO, and $Co_3O_4/P_{(2\%)}$rGO, respectively.

2.5 Characterizations

The phase purity levels and crystal structures of the synthesized flower-like Co_3O_4, P-rGO and flower-like Co_3O_4/P-rGO materials were investigated using an X-ray diffractometer (XRD, Rigaku Ultima IV, Japan) with Cu–K-alpha radiation and operating at a constant current of 40 mA and a constant voltage of 40 kV. The morphological aspect of the synthesized samples was investigated by a field emission scanning electron microscope (FESEM, ZEISS Gemini SEM, Germany) coupled with an Xmass detector for energy-dispersive X-ray spectroscopy (EDX) analysis to determine the elemental composition of the prepared samples. The Raman spectra were recorded using a micro-Raman spectrometer (Renishaw InVia Reflex 532) with an incident wavelength of 532.5 nm. The laser power was set to 0.1 mW to avoid potential damage or unexpected reductions due to laser irradiation. The graphene samples were placed on a background-free glass slide. The accumulation time of each spectrum was 100 s. To determine the chemical states of the elements and the electronic structure of the prepared composite. Thermo Scientific ESCALAB 250Xi XPS Microprobe, integrated with an Al Kα micro focusing X-ray monochromator, was used.

2.6 Electrode preparation

The electrode was prepared by the drop-casting method. Briefly, catalyst powder was used as an active material, and a binder and a solvent were used to fabricate the electrode. The binder's purpose was to ensure the active material remained on the electrode in the electrolyte solution. The working electrodes were prepared using a synthesized catalyst and binder with a wt% ratio of approximately 80 : 20. The polyvinylidene fluoride (PVDF) and DMSO were used as binder and solvent. To prepare the flower-like Co_3O_4 and Co_3O_4/P-rGO catalyst ink, 0.01 g of catalyst powder, 0.0024 g PVDF, and 160 μL DMSO were mixed and subjected to ultrasonic treatment at a power of 10 kHz for 30 min at room temperature (25 °C) to ensure uniform homogeneity. Subsequently, a calculated volume of the catalyst ink (*e.g.*, 20–40 μL) was drop-cast onto a pre-polished graphite disk electrode in an area of 0.52 cm^2 to achieve a catalyst loading of 0.5 mg cm^{-2}. The electrodes were dried in a vacuum oven at 50 °C for 12 h. Now, the dried electrodes were ready for electrochemical characterization, as shown in schematic Fig. 1.

2.7 Electrochemical performance analysis

To evaluate the electrochemical response for CO_2 reduction, a standard three-electrode setup was employed in an electrochemical H-type cell where the prepared electrode served as the working electrode (WE), Pt wire as a counter electrode (CE), and Ag/AgCl (3 M KCl) as the reference electrode (RE). The two compartments (anodic and cathodic) of the electrochemical H-type cell were separated by a proton exchange membrane (Nafion-117) to control the back oxidation of the counter electrode in the anodic compartment. All measurements were performed in a 0.5 M NaHCO3 aqueous solution, which served as the electrolyte. The electrocatalytic performance of the prepared electrode was measured using a CHI-660D electrochemical workstation. To investigate the electrocatalytic characteristics of CO_2 reduction, the reduced current density of the catalyst in a CO_2 medium was initially measured by using linear sweep voltammetry techniques. Linear sweep voltammetry was conducted in a 0.5 M $NaHCO_3$ solution, which was saturated with N_2 and CO_2 by bubbling for 2 h before the experiment. Linear sweep voltammetry measurements were implemented in a conventional three-electrode cell where a prepared electrode was used as the WE, Ag/AgCl (3 M KCl) as the RE, and Pt wire as the CE with a scan rate of 30 mV s^{-1}. To evaluate the electrocatalytic reduction of CO_2, chronoamperometry was performed at a fixed potential. Chronoamperometry is a similar process of electrolysis conducted in a gas-tight two-compartment (anodic and cathodic) electrochemical H-cell with a Nafion-117 membrane as a proton exchanger or separator. Both compartments (anodic and cathodic) have the same electrolyte (0.5 M $NaHCO_3$). Each compartment of the electrochemical H-cell had a 25 mL solution with approximately 20 mL headspace at a fixed potential. Before the electrolysis, the prototype H-type cell was flushed by bubbling N_2 and CO_2 for 30 min. During the

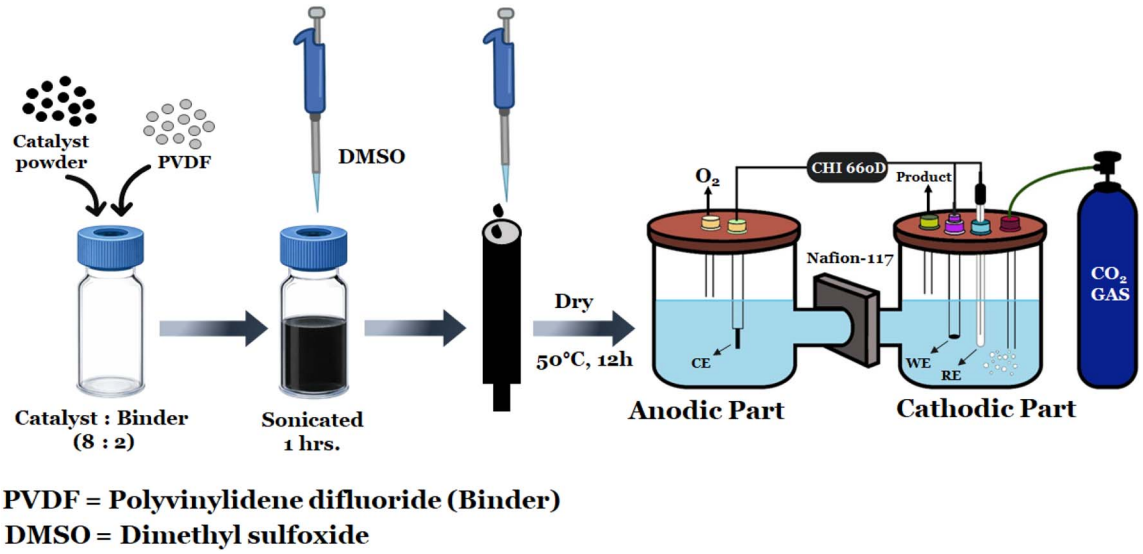

Fig. 1 Fabrication of the electrode.

electrolysis, the CO_2 gas was continuously purged in a cathodic compartment with a constant flow rate, followed by the electrolysis time. The electrochemical setup is depicted in Fig. 2.

After completing the electrolysis, a small fraction of electrolyte was collected by a syringe and analyzed using GC-FID (6890 series GC system, Agilent Technologies Co.). The calculation of faradaic efficiency was figured out by performance (SI) for the electrochemical reduction of CO_2 according to this equation.[47]

$$\%FE = \frac{nFZ}{Q} \times 100 \quad \text{(i)}$$

where, n = number of moles of the product. Z = numbers of electrons required to produce that given product. F = Faraday constant. Q = the total charge released.

3. Results and discussion

Before evaluating the electrocatalytic activity for CO_2 reduction, the structural, optical, and elemental properties of the synthesized catalysts were assessed using XRD, FESEM, EDX, Raman, and XPS. The crystallinity and purity of the synthesized materials were characterized by XRD analysis, as shown in Fig. 3.

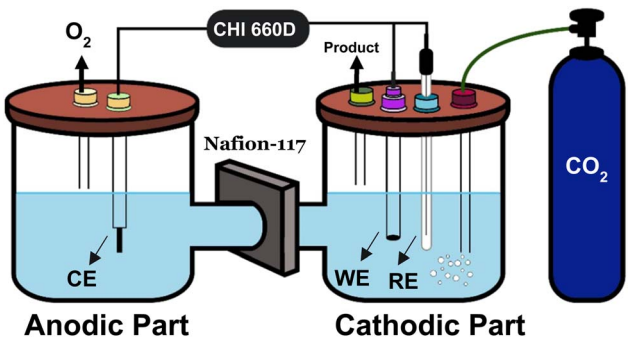

Fig. 2 Schematic diagram of the electrochemical setup for CO_2 reduction.

Fig. 3(a) demonstrates that P-doped rGO exhibits a sharp diffraction peak at $2\theta = 24.18°$ and $2\theta = 43.5°$ corresponding to (002) and (100) planes, respectively. Ordinary GO displays a diffraction peak, $2\theta = 10.6°$ for the (002) plane (Fig. S2).[48] Upon chemical or thermal reduction, the oxygen-containing groups are removed, resulting in a broader peak at $2\theta = 24.10°$ for rGO. However, the synthesized P-rGO material shows a diffraction peak at $2\theta = 24.18°$, indicating that the π-conjugated structure of graphene has been restored considerably by the production of rGO.[49] Additionally, a weaker peak at $2\theta = 43.5°$ corresponds to the (100) plane, attributed to the turbostratic band of disordered carbon materials.[50]

Fig. 3(b) presents peaks of 19.11°, 31.65°, 36.92°, 38.61°, 45.19°, 55.89°, 59.42°, and 65.3°, corresponding to the flower-like Co_3O_4 with crystalline planes (110), (220), (311), (222),

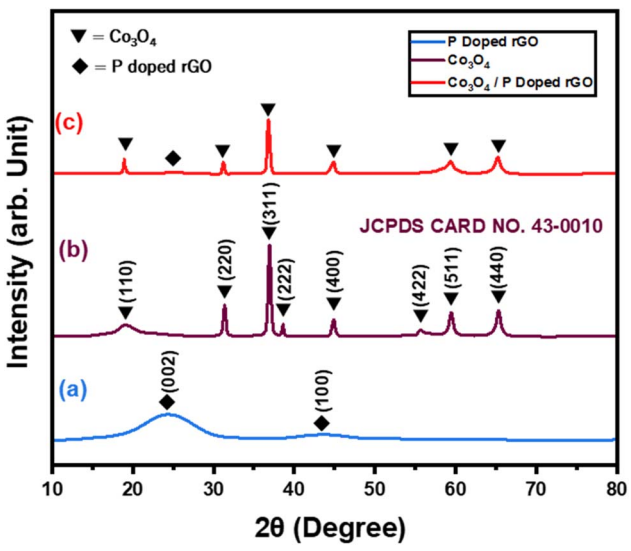

Fig. 3 XRD of (a) P-doped rGO, (b) flower-like Co_3O_4, and (c) flower-like Co_3O_4/P-rGO.

(400), (422), (511), and (440), respectively. The XRD peaks for shape-controlled Co_3O_4 exhibit a strong correlation with the data from the JCPDS card no. 43-0010.[51] This symbolizes that the pure shape controlled Co_3O_4 is formed without any impurities. The Fig. 3(c) describes the shape controlled Co_3O_4/P-rGO hybrid material consist the diffraction peak (2θ) of 19.11°, 31.65°, 36.92°, 45.19°, 59.42° and 65.3° represent the crystal plane (110), (220), (311), (400), (511) and (440) respective to shape controlled Co_3O_4 which was finely attributed with the JCPDS card no. 43-0010. Additionally, an extra diffraction peak was observed at 24.6° with the (002) plane, which was ascribed to disordered stacked graphitic sheets coordinated with the P-doped rGO XRD pattern that was earlier mentioned in Fig. 3(a).[52] This indicates that all the diffraction peaks were assigned with the structural formation of flower-like Co_3O_4/P-rGO hybrid composite, similar to both JCPDS card no (43-0010) and card no (41-1487) for individual shape-controlled Co_3O_4 and P-rGO component.

The average crystalline size of synthesized P-rGO, Co_3O_4, Co_3O_4/P-rGO was calculated by the Debye Scherrer equation.[53] As

$$D = \frac{\lambda K}{\beta \cos \theta} \quad \text{(ii)}$$

where, $K = 0.9$ is Scherrer's constant, λ is the wavelength of X-rays, θ is the Bragg diffraction angle β is the full width at half-maximum (FWHM) of the diffraction peak corresponding to the plane.

A distinct broadening of XRD peaks indicates that the material prepared is composed of a structure on the nanometer scale. The average crystalline size of GO, P-rGO, Co_3O_4, Co_3O_4/P-rGO is 4.54 nm (Fig. S2), 1.54 nm, 15.01 nm, and 14.79 nm, respectively. A slightly smaller crystallite size was observed for the hybrid Co_3O_4/P-rGO compared to pristine Co3O4, indicating the incorporation of P-rGO. Also, the interplanar spacing or *d*-spacing of synthesized materials is determined by Bragg's equation. The equation is,

$$n\lambda = 2d \sin \theta$$

$$d = \frac{n\lambda}{2 \sin \theta} \quad \text{(iii)}$$

where, n is the order of the diffraction peak, λ is the wavelength of X-rays, θ is the Bragg diffraction in radians, and d is the interplanar distance or d spacing. The interlayer spacing of synthesized materials GO, P-rGO, Co_3O_4, and Co_3O_4/P-rGO was found to be 0.61 nm, 0.28 nm, 0.26 nm, and 0.23 nm, respectively. This indicates a decrease in the shape controlled Co_3O_4/P-rGO hybrid material compared to pristine Co_3O_4 and P-rGO substrate. This is because the P-rGO aids in the segregation and dispersion of Co_3O_4 particles during the synthesis, facilitating the formation of the hybrid composite, as mentioned in the SEM images in Fig. 4(h).[54,55]

Surface morphology of the synthesized Co_3O_4, P-rGO, Co_3O_4/P-rGO materials was analyzed using FESEM, as shown in Fig. 4. Morphological attributes are influenced by crystallization, resulting in diverse structural shapes and sizes. Fig. 4(a–d) illustrates the shape-controlled Co_3O_4, which exhibits a distinct flower-like microstructure. These structures were composed of relatively uniform, self-assembled sheets that form petal-like subunits. At higher magnification, the petal-like structure consists of thin micro-sheets, contributing to the flake-like texture of each petal. The average diameter of these flower-like Co_3O_4 microstructures is approximately 4 μm, with a size distribution ranging from 2 μm to 8 μm. The length of the petal-like sub-units, which extended into micro sheets, was exhibited on a micro scale. The average length of the petal-like subunits extending from the flower's center was 1.3 μm. As observed in Fig. 4(d), the petal-subunit length lies in the micrometer range, with the edges tapering to the nanometer scale. Fig. 4(e and f) depicts the morphology of P-doped rGO material, which exhibits crumpled, sheet-like structures resembling cabbage leaves. The wrinkled surface was attributed to the high-temperature hydrothermal treatment applied to the synthesized P-doped rGO from GO. The rough and multilayer texture confirms the successful incorporation of P into rGO structures. On the contrary, Fig. 4(g and h) represents the morphologies of flower-like Co_3O_4/P doped rGO hybrid material, where the flower-like Co_3O_4 is anchored on the layer-structured P-doped rGO sheets. Unlike the pristine Co_3O_4, the flower diameters and their petal subunits in the hybrid Co_3O_4/P-rGO composite are notably smaller, falling within the nanometer scale as shown in the higher magnification in Fig. 4(h). The size reduction is likely due to P atom doping, which modifies the charge density at the graphene surface, as confirmed by XRD analysis (Fig. S2).

Additionally, partially disrupted flower centers observed on the P-rGO sheets were likely due to the coordination of Co^{3+} ions with negatively charged phosphorous-containing functional groups on the rGO sheets. During the ultrasonication process, Co^{2+} ions were oxidized to Co^{3+} by oxygen-containing groups, leading to the crystallization of Co_3O_4 particles that subsequently nucleated and anchored onto the P-rGO sheets.[56] While this mechanism aligns with the observed particle size and distribution, it should be considered a speculative interpretation rather than a confirmed mechanism, given the known role of defect-rich, heteroatom-doped carbon materials in providing nucleation sites for metal species.

The EDX analysis of Co_3O_4, P-doped rGO, and Co_3O_4/P-rGO materials was presented in Fig. 5. The EDX spectra provide qualitative and quantitative information about the chemical composition of a material.[56] The Co_3O_4 sample showed Co and O atom percentages of 26.12% and 73.88%, respectively. EDX mapping confirmed the exclusive presence of Co and O, with no detectable impurities (Fig. S3). The P-rGO material contained C(81.05%), O (17.70%), and P(1.25%) in P-rGO, respectively (Fig. S4), confirming successful doping of P onto the rGO matrix. Although EDX does not reveal the information of chemical bonding, it gives the elemental composition of materials in mass and atom percentage.[57] EDX spectra of the Co_3O_4/P-rGO hybrid showed the presence of Co, C, O, and P with atom percentages of 11.03%, 48.52%, 39.31% and 1.01%,

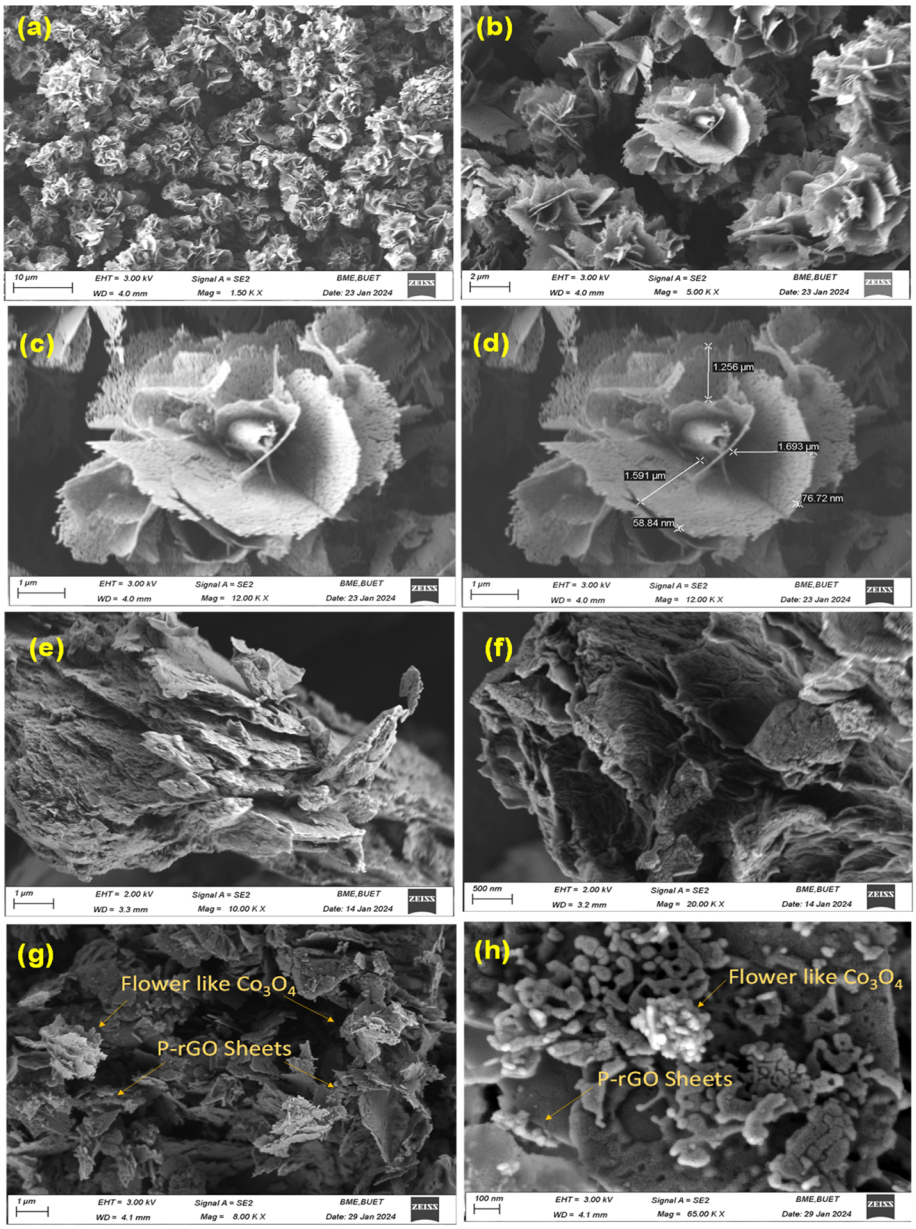

Fig. 4 FESEM images of (a–d) flower-like Co_3O_4 (e and f) P-doped rGO (g and h) composite of Co_3O_4/P-rGO.

respectively. Elemental mapping confirmed the spatial distribution of these elements, where Co derived from the Co_3O_4 anchored on the surface of the P-rGO, C originated from the rGO, O from both the rGO and the Co_3O_4 materials, and P from the doped rGO, confirming the material's high purity and successful synthesis.

The Raman spectra of Co_3O_4 and the Co_3O_4/P-rGO composite are shown in the Fig. 6(a) and (b), respectively, while the spectra of GO, rGO, and P-doped rGO are provided in Fig. S5. Five characteristic vibrational modes were observed in Fig. 6(a) for pristine Co_3O_4 at approximately 191, 470, 510, 608 and 695 cm^{-1}, which are in good agreement with reported Raman-active modes of spinel Co_3O_4. The intense peak at 695 cm^{-1} corresponds to the A_1g mode, associated with the symmetric stretching of the oxygen atom in CoO_6 octahedra, confirming the formation of a well-crystallized spinel structure. The Raman spectra of GO, rGO, and P-rGO display the characteristic D (1350) and G (1580) bands. The calculated I_D/I_G ratios for GO, rGO, and P-rGO are 1.37, 1.27, and 0.90, respectively (Fig. S5). The progressive decrease in I_D/I_G ratio from GO to rGO indicates a partial restoration of the sp^2 carbon network and a reduction in structural defects during the reduction process. A further decrease for P-rGO indicates the phosphorous doping promotes structural reorganization resulting in an increase in the average size of sp^2 domains and a more continuous conjugated carbon framework.

For Co_3O_4/P-rGO, the coexistence of Co_3O_4 vibrational modes and the D and G bands confirms the successful formation of the hybrid structure, as shown in Fig. 6(b). The I_D/I_G ratio of the hybrid Co_3O_4/P-rGO is 1.04, which lies between those of

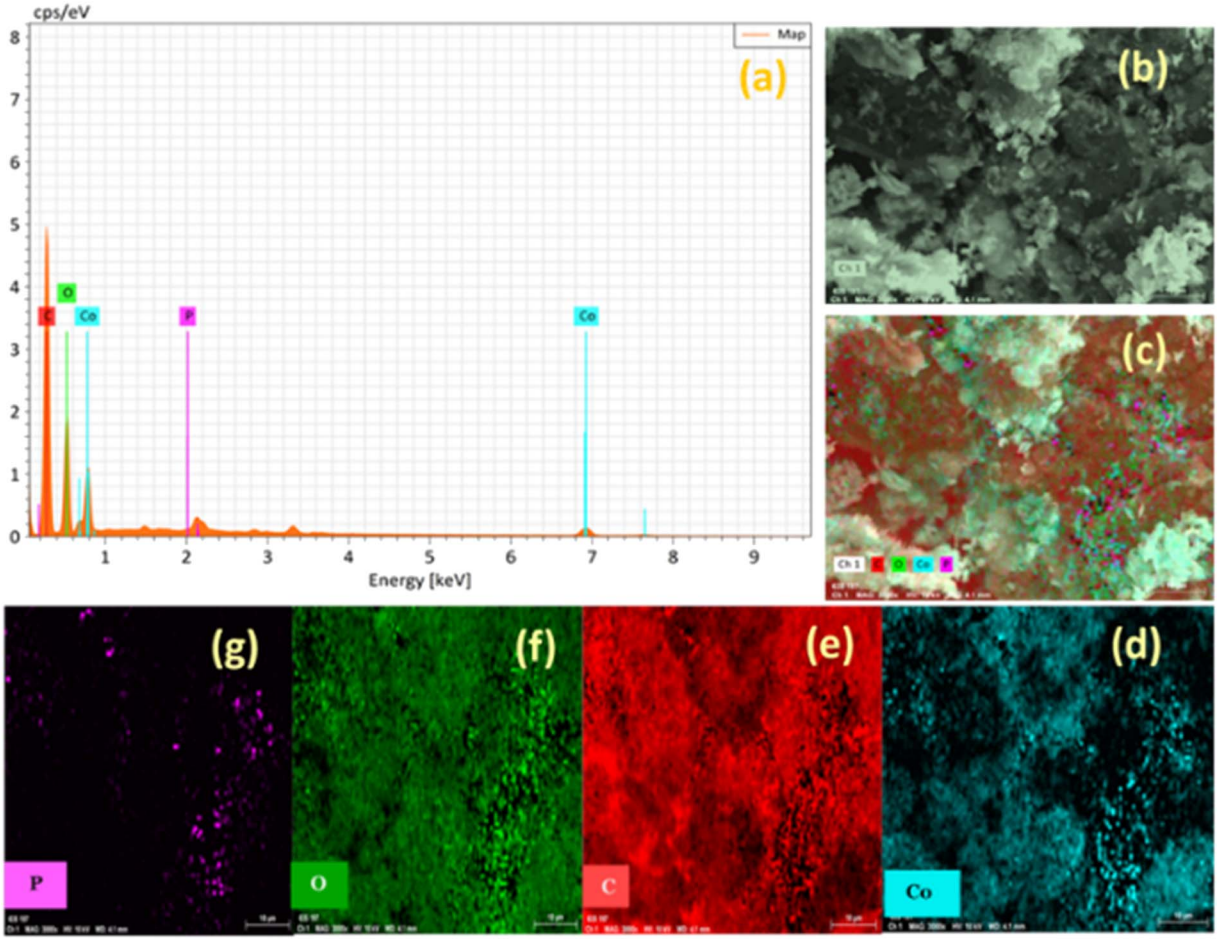

Fig. 5 EDX analysis of Co_3O4/P-rGO; (a) elemental spectrum (b and c) EDX mapping of selected area of identifying Co, P, C, O elements; (d) Co elements (e) C elements (f) O element (g) P element.

Co_3O_4 and P-rGO. This enhancement in defects can be attributed to strong interfacial interactions between Co_3O_4 and the P-rGO, which induce structural distortion and generate additional defect sites. Additionally, a slight red shift in the D and G bands is observed after composite formation, indicating electronic interaction between Co_3O_4 and the P-rGO support. This shift can be attributed to charge transfer effects and lattice strain induced by the anchoring of Co_3O_4 onto the P-rGO surface.

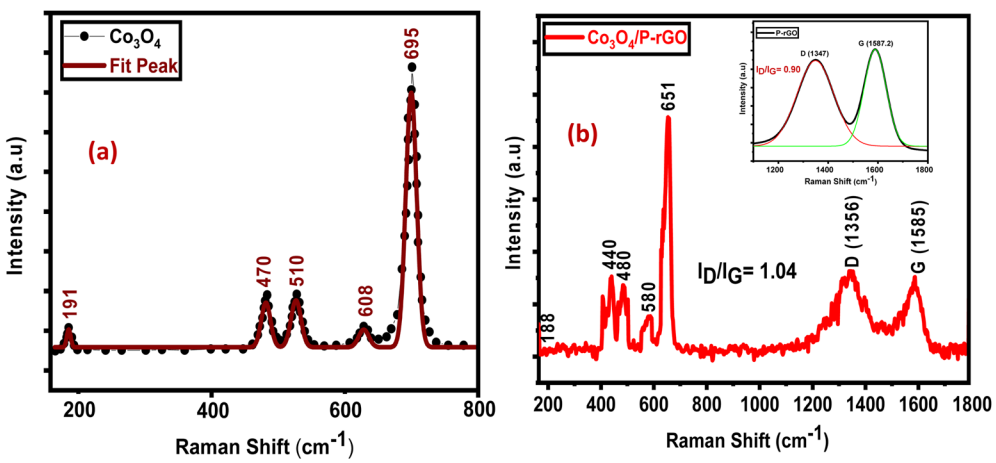

Fig. 6 Raman spectra of (a) flower-like Co_3O_4 (b) flower-like Co_3O_4/P-rGO.

X-ray photoelectron spectroscopic (XPS) analysis was performed to determine the surface elemental composition, electronic structure, and deconvoluted spectra of Co_3O_4/P-rGO hybrid material. Fig. 7(a) demonstrates the survey spectrum of the prepared Co_3O_4/P-rGO hybrid material consisting of C, O, P, and Co elements. The rGO sheets were accumulated in a synthesized Co_3O_4/P-rGO hybrid material, which was also confirmed by the survey spectrum in Fig. 7(a) and the

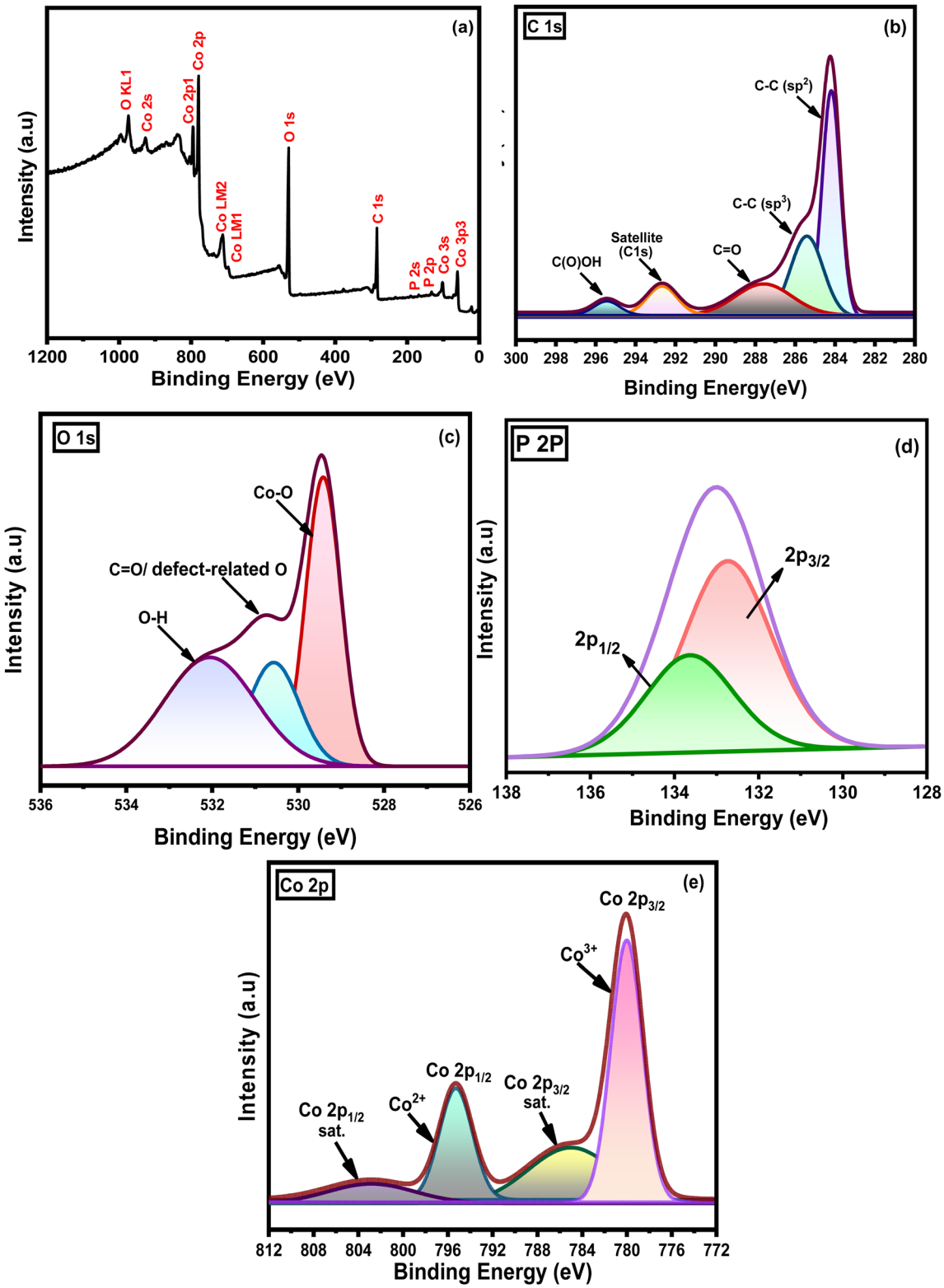

Fig. 7 XPS images of (a) survey spectra of Co_3O_4/P-rGO; (b–e) survey scan of (b) C 1s, (c) O 1s, (d) P 2p, and (e) Co 2p.

asymmetric deconvolution of the carbon C(1s) spectra of Fig. 7(b). The C(1s) spectra exhibit five distinct peaks of deconvoluted positioned at 284, 285, 288, 292 and 295 eV which are attributed to sp^2 hybridized C–C in aromatic rings, epoxy/ether group (C–O), sp^3 hybridized C–C/C–H bonds and a shake-up satellite peak ($\pi \rightarrow \pi^*$) as a characteristic of aromatic C structures and carboxylic group (O–C=O), respectively.[58,59] These spectral features indicate a shift in the binding energies of oxygenated functional groups, along with the successful incorporation of P dopant in the prepared hybrid material. The observed shift of these oxygenated groups creates a strong interaction to anchor the shape-controlled Co_3O_4 with the functional groups of P-rGO material.[60] Furthermore, the deconvoluted peak of oxygen O(1s) from Fig. 7(c) yields three peaks centered at 529, 530, and 532 eV corresponding to the Co–O bond in the metal oxide lattice, oxygen-deficient sites (vacancies) or C=O, and chemisorbed oxygen anions or oxygen related to OH ions, respectively.[61] The binding energies of O(1s) confirmed that the defect sites are formed in the synthesized flower-like Co_3O_4/P-rGO hybrid material. The high-resolution P 2p XPS spectrum exhibits two characteristic peaks at approximately 132 and 133 eV, corresponding to P $2p_{3/2}$ and P $2p_{1/2}$, respectively. These peaks are attributed to phosphorus atoms in the phosphate group, as shown in Fig. 7(d).[62,63] The XPS spectrum in Fig. 7(e) reveals that the two main peaks positioned at 780, and 795 eV respectively consist of $CO_{2p_{3/2}}{}^{3+}$ and $CO_{2p_{1/2}}{}^{2+}$ oxidation state with two satellite peaks located at 785 and 803 eV.[64] The chemical state is also determined by measuring the difference between two spin separation energies between $CO_{2p_{3/2}}{}^{3+}$ and $CO_{2p_{1/2}}{}^{2+}$. Deconvolution of these peaks indicates contributions from both Co^{3+} and Co^{2+} species, consistent with the coexistence of mixed valence states in the Co_3O_4/P-rGO composite. For instance, the spin–spin splitting between $CO_{2p_{3/2}}{}^{3+}$ and $CO_{2p_{1/2}}{}^{2+}$ is 15 eV signifies low spin Co^{3+} species, are present in composite phase.[65] Additionally, the two corresponding satellite peaks positioned at 803 and 785 eV for Co $2p_{1/2}$ and Co $2p_{3/2}$, correspond to the Co^{2+} species. That means, a portion may be attributed to reducing Co^{3+} to Co^{2+} and creating oxygen vacancies.

Linear sweep voltammetry (LSV) was conducted to evaluate the electrocatalytic reduction of CO_2 on the prepared cathode electrodes. LSV was carried out in both N_2 and CO_2 saturated 0.5 M $NaHCO_3$ aqueous solution as an electrolyte at a scan rate of 30 mV s^{-1} in a typical three electrode system, where Ag/AgCl (3 M) was used as a RE, platinum wire as a CE, and the prepared catalyst was used as the modified WE. The pH was maintained in N_2, and CO_2-saturated 0.5 M $NaHCO_3$ aqueous solutions were 8.5 and 7.5, respectively. Each system was cycled 15 times over a potential range of −0.2 to −1.05 V at a scan rate of 30 mV s^{-1} to stabilize the electrode response. Fig. 8(a) displays relatively low reduction currents under N_2, while Fig. 8(b) highlights a substantial increase under CO_2, confirming the catalyst's activity in CO_2 reduction. The bare graphite electrode showed a negligible current in N_2, but a significant increase in current was observed from −0.6 V in the presence of CO_2. By modifying the graphite electrode using P-rGO, flower-like Co_3O_4 and flower-like Co_3O_4/P-rGO catalyst, the cathodic current densities under N_2 were −1.04, −2.42, −9.58 and −11.70 mA cm^{-2}, respectively, due to proton/water reduction. In contrast, under CO_2-saturated conditions, the current was increased with the P-rGO, Co_3O_4, and Co_3O_4/P-rGO catalyst by modifying the graphite electrode. From Fig. 8(b), the decreasing current in CO_2 conditions was found to be −3.82, −5.75, −14.77, and −19.15 mA cm^{-2}, respectively, for graphite and graphite modified with P-rGO, Co_3O_4, and Co_3O_4/P-rGO cathode electrodes. Fig. 8(a) and (b) shows that both the set data of N_2 and CO_2 conditions with a single graphite electrode and the modified electrode with P-rGO, Co_3O_4, and Co_3O_4/P-rGO catalyst had a drastic change in reduced current. These observations indicate that the presence of CO_2 significantly enhances the reduced current, with the current densities increasing by factors of approximately 2, 3, 5, and 8 for P-rGO, Co_3O_4, and Co_3O_4/P-rGO

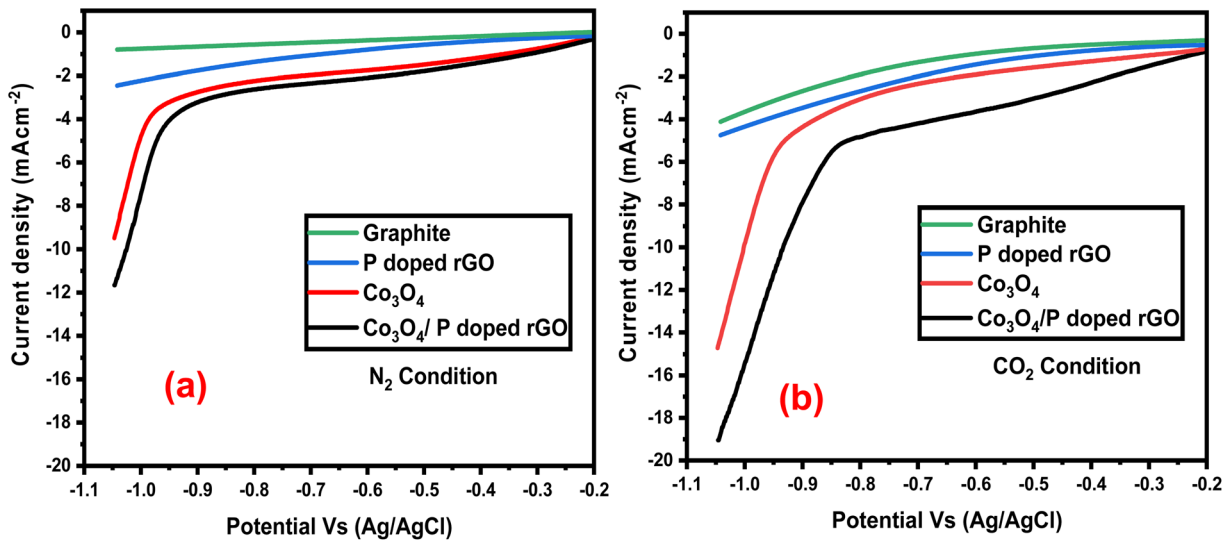

Fig. 8 LSV of prepared catalyst (a) N_2 condition, (b) CO_2 condition, in 0.5 M $NaHCO_3$ aqueous solution at 30 mV s^{-1} scan rates.

catalysts, respectively, compared to N_2 conditions. Thus, the enhancement of reductive current indicates that the catalytic activity of the modified electrode using P-rGO, Co_3O_4, and Co_3O_4/P-rGO catalysts can reduce CO_2. The LSV data clearly demonstrate the superior electrocatalytic performance of the synthesized flower-like Co_3O_4/P-rGO composite, outperforming its individual entities, indicating that a synergistic effect between the two materials is effective for the electrocatalytic reduction of CO_2.

The catalyst utilizes a metal–organic framework-based WE, featuring flower-like Co_3O_4 as the metal framework and rGO as the organic framework. Following the phosphorus doping into rGO substrates and binding with Co_3O_4, the catalytic performance of the resulting Co_3O_4/P-rGO hybrid structure has greatly improved by varying the amount of P that has been doped. LSV was used to investigate the catalytic performance of Co_3O_4/P-rGO hybrids with varying P doping ratios. The P doping levels in the heterostructures were precisely adjusted to 0.5%, 1%, and 2%. Fig. 9(a) and (b) show that an increase in the P doping ratio led to a higher reduction current, with increments of −11.52, −18.51, and −15.36 mA cm^{-2}, and Tafel slopes of 80, 60, and 20 mV dec^{-1}, respectively. Catalytic performance was evaluated by comparing the potentials at which specific current densities were achieved according to the RHE, as shown in Fig. 9(a). The kinetic parameters of CO_2 reduction in different electrodes were calculated according to the given equations,[66]

$$\eta = a + b \log i$$

where, η is the overpotential (volts), i is the current density (mA cm^{-2}), a is the Tafel constant (often related to the exchange current density) and b is the Tafel slope (mV per decade).

In Fig. 9(b), the catalyst was prepared using a metal–organic framework-based working electrode, featuring flower-like Co_3O_4 as the metal framework and rGO as the organic framework. Phosphorus doping into the rGO substrate and its interaction with Co_3O_4 significantly enhanced the catalytic performance of the resulting Co_3O_4/P-rGO hybrid. The P doping levels were precisely controlled at 0.5%, 1%, and 2%. The catalytic performance of the Co_3O_4/P-rGO hybrids was investigated using LSV, as shown in Fig. 9(a). Increasing the P content from 0.5% to 1% increased the reduction current from −11.52 to −18.51 mA cm^{-2}, while further increasing P to 2% led to a slight decrease to −15.36 mA cm^{-2}.

Tafel plots in Fig. 9(b) were used to evaluate the reaction kinetics. The Tafel slope decreased sharply from 80 mV dec^{-1} at 0.5% P to 20 mV dec^{-1} at 1% P, indicating accelerated electron transfer and enhanced catalytic kinetics. However, at 2% P, the Tafel slope increased again to 60 mV dec^{-1}, likely due to overdoping that caused partial active-site blockage or structural distortion. A smaller Tafel slope corresponds to faster kinetics, enabling the catalyst to achieve higher current densities under moderate applied potentials. The Tafel slope provides a reliable measure of kinetic efficiency without the need for explicit overpotential calculations.[66,67] Based on these analyses, the $Co_3O_4/P_{(1\%)}$-rGO hybrid exhibited the lowest Tafel slope and best overall CO_2 reduction performance, and was therefore selected for further characterization (XRD, FESEM, XPS, and EDX) and electroreduction studies. The Tafel slope shows a significant dependence on the P doping level. Increasing the P content from 0.5% to 1% results in a sharp decrease in the Tafel slope from 80 mV dec^{-1} to 20 mV dec^{-1}, indicating enhanced catalytic kinetics. However, a further increase to 2% lead to an increase in Tafel slope again to 60 mV dec^{-1}. A smaller Tafel slope signifies accelerated electron transfer and faster catalytic kinetics, allowing the catalyst to reach high current densities more readily under moderate applied potentials.[67] These findings demonstrate that a 1 wt% P doping yields the lowest absolute Tafel slopes, which is the smallest (20 mV dec^{-1}), offering the best CO_2 reduction performance and excellent stability. On the other hand, the performance drop at 2% P doping may be due to overdosing, leading to active-site blockage or structural distortion. Based on this optimization, the hybrid flower-like $Co_3O_4/P_{(1\%)}$-rGO structure was selected for further

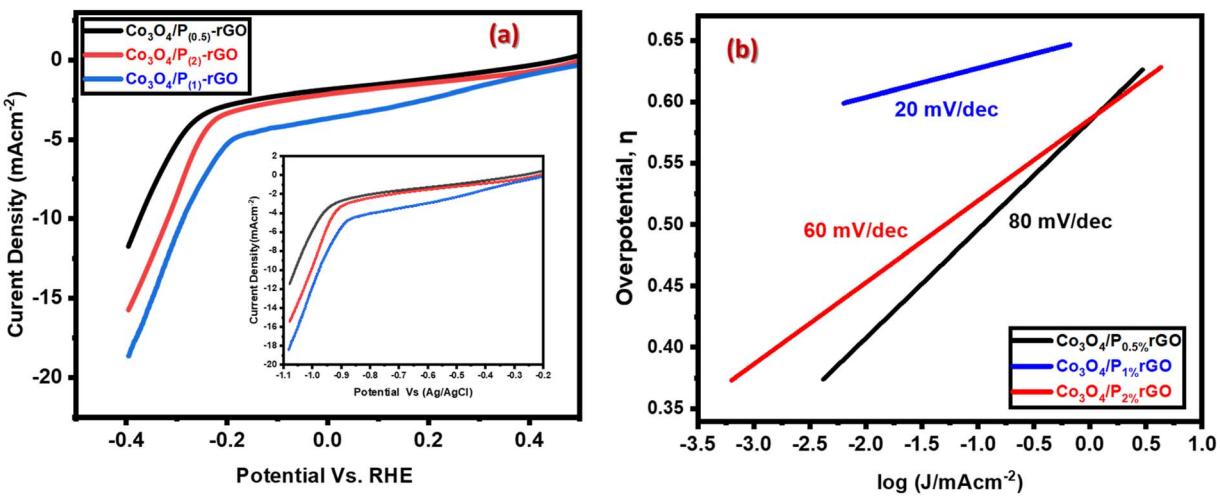

Fig. 9 Comparison of the CO_2RR performance (a) LSV analysis (b) Tafel plots for different amounts of dopant composition to hybrid materials.

material characterization (XRD, FESEM, XPS, and EDX) and CO_2 electroreduction applications.

Since both water and CO_2 can be reduced under such conditions, LSV alone is insufficient to assess electrocatalytic activity for CO_2 reduction.[68] Therefore, potentiostatic electrolysis or chronoamperometry was performed in a CO_2-saturated 0.5 M $NaHCO_3$ aqueous solution (pH value 7.5) at a constant of −0.62 V in an H-type electrochemical cell for 2.5 hours. The resulting liquid-phase products were analyzed using gas chromatography-mass spectrometer (GC-MS, Clarus 680). The selection of the applied potential for CO_2 conversion was guided by Tafel plot analysis, which identified an apparent equilibrium potential and the kinetically favorable region for CO_2 reduction.[69] CO_2 was continuously purged at a flow rate of 10 mL min^{-1} in the cathodic chamber, with a regulator-maintained pressure of 362 psi (0.06 bar) from the gas cylinder, which was separated from the anodic chamber by a Nafion-117 membrane, as shown in Fig. 10(b). A constant voltage (−0.62 V) was applied for different modified electrodes. The chronoamperometry was taken in an H-type electrochemical cell using Ag/AgCl as RE. From LSV data, a notable increase in current density was observed beginning at −0.6 voltage (*vs.* Ag/AgCl) in LSV data for the flower-like Co_3O_4 electrode. Furthermore, after analyzing the Tafel plot (Fig. S7) for CO_2 reduction, the −0.6 V selected for product selectivity is adjusted to −0.62 to ensure an adequate driving force for CO_2 reduction while remaining within the kinetically favorable region.

Potentiostatic measurements were conducted on Co_3O_4 and Co_3O_4/P-rGO electrode, prepared by modifying a graphite substrate. A stable current density was exhibited, approximately −0.5 mA cm^{-2}, while the flower-like Co_3O_4/P-rGO hybrid material maintained a consistent current density of −0.8 mA cm^{-2} at the same potential. The total charge released, or the number of electrons introduced during this chronoamperometric process, which is essential for estimating the faradaic efficiency, was determined by integrating the current–time (I/t) curve over the course of the experiment.[70] The charges released for the Co_3O_4 and Co_3O_4/P-rGO modified electrode for a 2.5-hour electrolysis time were found to be 1.85C and 3.65C, respectively. Comparing the current density and the amount of charge released for both the Co_3O_4 and Co_3O_4/P-rGO electrodes, at a fixed potential, both the cathodic current density and the released charge amount increase. This indicates that the synthesized Co_3O_4 and Co_3O_4/P-rGO modified electrodes exhibit effective cathodic behavior. The synthesized Co_3O_4 and Co_3O_4/P-rGO materials worked as a cathode and showed very stable operation for the electrocatalytic reduction of CO_2 under a constant applied potential.

After completing the electrolysis, the resultant liquid products were analyzed using a Clarus 680 gas chromatography-mass spectrometer (GC-MS). The faradaic efficiency of the produced product was determined using a modified graphite electrode with Co_3O_4 and Co_3O_4/P-rGO catalysts under a constant applied voltage of −0.62 V, as illustrated in Fig. 11. The current density from the chronoamperometric (Fig. 10) measurements reflects sustained product formation over a long period of electrolysis. Although hydrogen evolution is recognized as a competing reaction in CO_2 reduction systems, accurate quantification of H_2 was not feasible because of limitations in gas collection and trapping during electrochemical measurements. The Co_3O_4 catalyst achieved a faradaic efficiency of 69% for ethanoic acid (SI), which was confirmed by GC-MS. In contrast, the hybrid Co_3O_4/P-rGO yielded a product mixture of ethanoic acid and propanal, with faradaic efficiency of 58% and 9%, respectively (SI). As the electroreduction of CO_2 is pH sensitive, for the detection of electrolyte from GC-MS, the pH was found 7.1 ± 0.2.

As shown in Fig. 11, the use of Co_3O_4 alone predominantly yields a single liquid derivative, ethanoic acid, at 69% faradaic efficiency. However, when the Co_3O_4 and P-rGO were hybridized, the product selectivity changed. For the composition of flower-

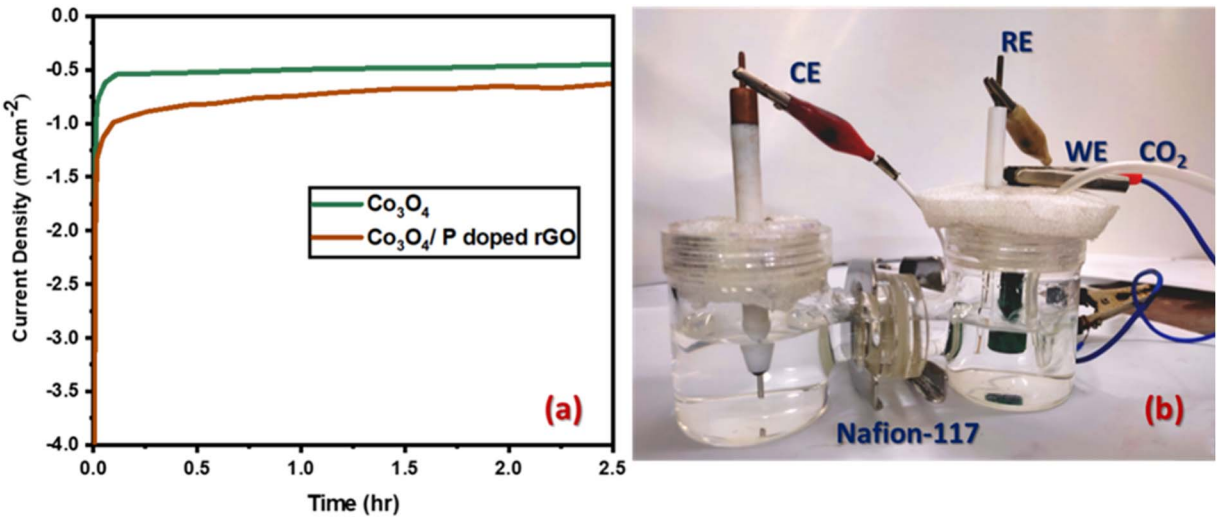

Fig. 10 Chronoamperometry response for CO_2 electroreduction for (a) prepared Co_3O_4 (green line) and Co_3O_4/P-rGO (brown line) catalyst at −0.62 V in H-type prototype; (b) setup for chronoamperometry process.

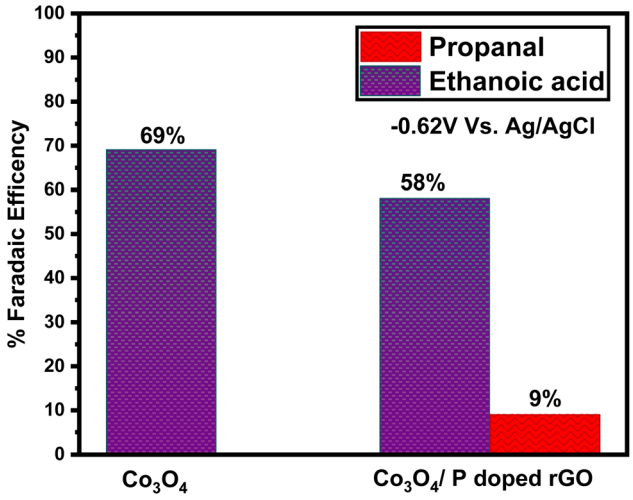

Fig. 11 Study of the faradaic efficiency of produced product *versus* electrolysis voltage as prepared catalyst Co_3O_4 and Co_3O_4/P-rGO in 0.5 M $NaHCO_3$ aqueous solution.

like Co_3O_4/P-rGO, the $\%FE_{CH_3COOH}$ is decreased to 58% from 69% of the individual flower-like Co_3O_4 catalyst. Also, propionaldehyde or propanal is observed, with a faradaic efficiency of 9%. These findings indicate that the P-rGO materials give an effective electron transport capacity and facilitate the proton-coupled with the multielectron transfer of CO_2 electroreduction reactions for the hybrid flower-like Co_3O_4/P-rGO catalyst. Ethanoic acid is the primary product and dominant for the catalyst of both Co_3O_4 and Co_3O_4/P-rGO materials at the same voltage. Compared to pristine Co_3O_4 catalyst, the Co_3O_4/P-rGO hybrid exhibited a decreased faradaic efficiency ($\%FE_{CH_3COOH}$), while the formation of propanal was observed with a notable faradaic efficiency ($\%FE_{C_2H_5CHO}$) due to the synergistic effect between Co_3O_4 on P-rGO materials.

To verify the liquid-phase product formed by the electrocatalytic reduction of CO_2, GC-MS analysis was performed of the liquid electrolyte after electrolysis. Accurate product identification is essential for determining the effectiveness of the electrochemical method, including the catalyst, electrolyte, or overall reaction conditions. The mass spectra of the detected analytes were matched with the NIST spectral library (Table S2), and the quantification of liquid product was then performed by correlating the peak area with the calibration curve of the corresponding standard compounds (Fig. S8). As previously mentioned, ethanoic acid was detected as a major product when using a flower-like Co_3O_4 electrocatalyst. This was confirmed by the GC-MS spectrum shown in Fig. 12(a). The resulting GC-MS spectra in Fig. 12(a) consist of a base peak, which is the most abundant peak, and the characteristic fragments at $m/z = 60.87$ correspond to the acetic acid (CH_3COOH^+).[71] Additionally, it has a molecular ion peak and characteristic fragments at $m/z = 58.90$ for the CH_3COO^- fragment, along with an isotopic peak at $m/z = 61$, corresponding to $^{13}CH_3COOH^+$ or $CH_3{}^{13}COOH^+$.[72] In contrast, both ethanoic acid and propanal were also identified for the catalytic reduction of CO_2 using the flower-like Co_3O_4/P-rGO hybrid materials as shown in Fig. 12(b and c). The GC-MS spectrum in Fig. 12(b) attributed a molecular ion peak at $m/z = 60.87$, consistent with acetic acid (CH_3COOH^+), further validating its presence in the electrolyte. Meanwhile, the spectrum in Fig. 12(b) confirms the formation of propanal, with a base ion peak appearing $m/z = 56.87$, which contributes to the mass fragments of $C_3H_5O^+$ and a molecular ion peak at $m/z = 58$ for $C_3H_6O^+$.[73] The reduced intensity of this molecular ion peak in Fig. 12(b) indicates the coexistence of propanal in the electrolyte mixture.

Fig. 13 illustrates the electrocatalytic pathway for producing ethanoic acid and propanal from CO_2 reduction. CO_2 is reduced *via* proton-coupled electron transfer (PCET) steps. It undergoes reduction to form higher carbon selective C_2 and C_3 products. Acetic acid originates through the interaction between the $CO_2^{\bullet-}$ radical anion and the reduced ($-CH_3$) species adsorbed on the catalyst's surface.[74] The $CO_2^{\bullet-}$ radical anion first forms formaldehyde (HCHO), which can occour with or without a catalyst. The reaction proceeds with the reduction of $CO_2^{\bullet-}$, which either weakly adsorbed on the electrode surface or

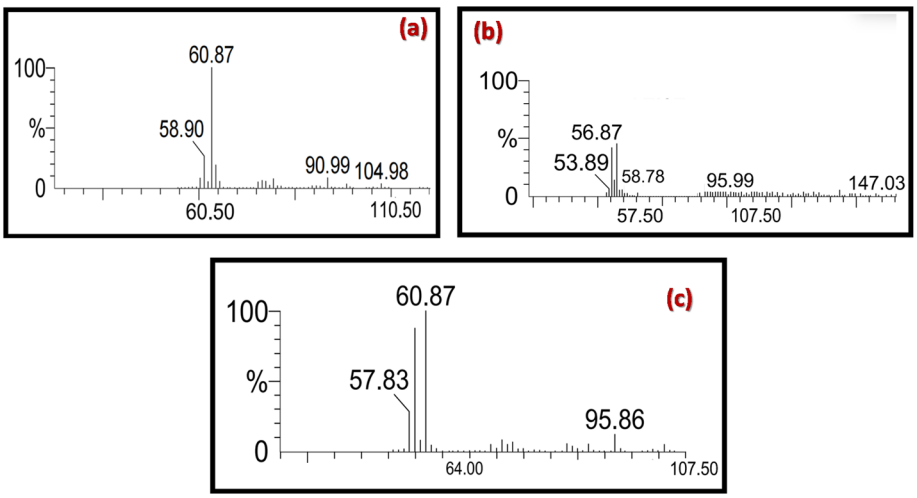

Fig. 12 GC-MS spectra of electrolyte solution after 2.5 h chronoamperometry *vs.* Ag/AgCl, pH 7.5 (a and b) ethanoic acid (c) propanal.

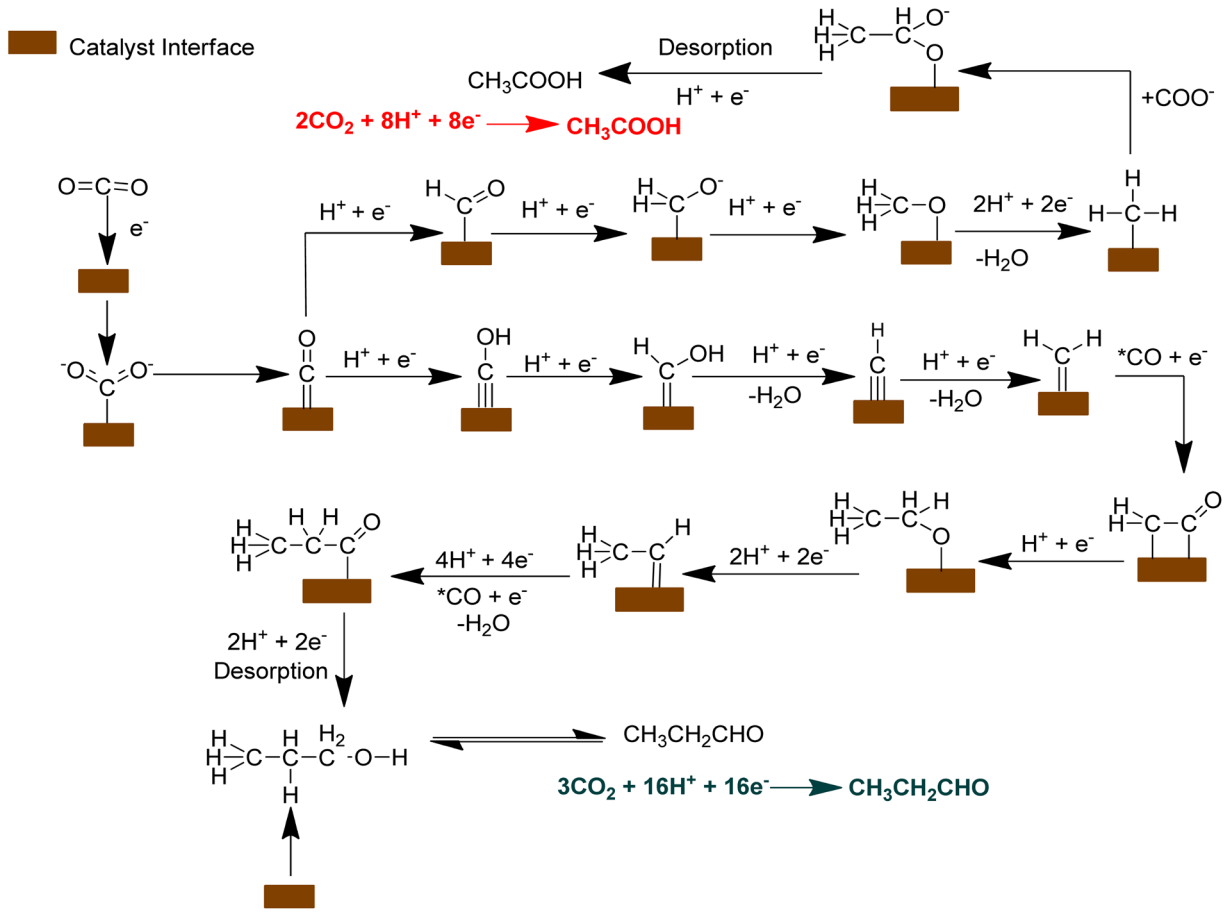

Fig. 13 Possible reaction pathways for the electrocatalytic CO_2 reduction to ethanoic acid (CH_3COOH) and propanal (CH_3CH_2CHO).

undergoes proton attack.[75] After adsorption, the C–O bond breaks, releasing a water molecule and forming an $-CH_2O$ intermediate. Further reduction produces the $-CH_3$ species, which serves as a precursor for acetic acid, occurring in a highly reducing environment, where electrons are supplied by the anode through an external circuit and the protons arrive at the cathode *via* the Nafion-117 membrane, which is in direct contact with the electrocatalyst. In the final stage, the C–O bond breaks in two stages, releasing water and forming ethanoic acid. This happens either *via* nucleophilic attack by non-adsorbed $CO_2^{\bullet-}$ or through the reaction between the adsorbed $-CH_3$ species and $CO_2^{\bullet-}$ at a nearby catalytic site.[76] Conversely, in the formation of propanal, the C–C–C bond formation is the key step for C_3 product. It would occur in two stages: C–C bond formation and post C–C coupling steps.[77] Fig. 13 demonstrates the potential pathways either the direct formation of the CO dimer, or CO reacting simultaneously with H^+ and e^- to generate the HCOH intermediate. While another pathway involves the protonation of CO to form –CHO, which is selective for methane and glyoxal products. However, at a very negative overpotential, CO dimerization is reportedly difficult.[78] As a result, CO is more likely to reduce to –COH, which then forms the HCOH intermediate. Subsequently, through proton–electron-coupled transfer and water elimination, the HCOH intermediate is transformed into $-CH_2$. The proton-coupled electron transfer serves as the rate-determining step in this pathway which implies that the process is influenced by pH. For C–C bonding formation, CO is inserted into $-CH_2$. It is found that the charged water layer could stabilize the CO dimer, and without charged water layer, the CO dimer formation is energetically prohibited. Due to CO insertion, the $-CH_2$ is then shifted to H_2CCO^-.[79] After the post coupling step of C–C, it is shown that protonation of the H_2CCO^- intermediate results in $CH_3CH_2O^-$, which are then further reduced to CH_3CH. Then CH_3CH group is subsequently reduced to form CH_3CO by the addition of hydrogen and electron transfer, breaking molecular bond, leading to the formation of the acetyl group. The reduction process may involve the conversion of CH_3CH which is further reduced to CH_3CO, acting as a precursor for C_3 products. The precursor CH_3CO is further converted to CH_3CHCHO^- due to the CO insertion, proton–electron-coupled transfer and water elimination.[80] Protonation into CH_3CHCHO^- intermediate converted $CH_3CH_2CH_2OH$ and desorb from the catalyst. As previously mentioned, the electroreduction of CO_2 is pH responsive, under specific conditions-including voltage, anodic materials, pH (7.1 ± 0.2) and the concentration of CO_2, the $CH_3CH_2CH_2OH$ is oxidized to CH_3CH_2CHO.

Table 1 CO_2 electroreduction performance of various Co_3O_4-based catalysts

Catalyst	Electrolyte	Shape	Potential	Product (%FE)	Stability	Ref.
Co_3O_4 Nanofiber	0.1 M $TBAPF_6$ in ACN + 1% vol H_2O	Nanofiber	−1.5 V *vs.* NHE	CO (65%) HCOOH (27%)	8 h	27
Co_3O_4 Ultrathin	0.1 M $KHCO_3$	Ultrathin	−0.88 V *vs.* SCE	HCOOH (60%)	20 h	82
Co_3O_4/N-GO Nano cube	0.1 M $KHCO_3$	Nano cube	−0.95 V *vs.* SCE	HCOOH (83%)	8 h	83
Crystal facet like Co_3O_4/rGO	0.5 M $KHCO_3$	Crystal facet tailored	−0.4 V *vs.* RHE	C_2H_5OH (45.9%) $H_2C{=}CH_2$ (28.8%)	6 h	28
Atomic Co layers	0.1 M Na_2SO_4	Nanosheet	−0.85 V *vs.* SCE	HCOOH (90%)	60 h	84
Co/CNT Polyhedral	0.5 M $KHCO_3$	Polyhedral	−0.7 V *vs.* RHE	CO (90%)	40 h	85
Cu_2O/rGO	0.1 M $KHCO_3$	Cubic Cu_2O anchored on rGO	−0.9 V *vs.* RHE	CO (70%)	1 h	86
P- and N-co-doped rGO	0.1 M $KHCO_3$	Dual dopants	−0.9 V *vs.* RHE	HCOOH (70%)	—	87 and 88
Flower-like Co_3O_4	0.5 M $NaHCO_3$	Flower	−0.62 V *vs.* Ag/AgCl	CH_3COOH (69%)	2.5 h	This work
Flower-like Co_3O_4/P-rGO	0.5 M $NaHCO_3$	Flower-like Co_3O_4 Anchored on the P-rGO sheet	−0.62 V *vs.* Ag/AgCl	CH_3COOH (58%) CH_3CH_2CHO (9%)	2.5 h	This work

Materials like platinum, gold, or carbon-based electrodes are commonly used for alcohol oxidation.[81] In this case, the platinum wire is used as an anode, which is highly effective for oxidizing alcohols to aldehydes, with high activity and stability. It is reasonable to predict that propanol is oxidized to propanal, releasing protons and electrons. This transformation occurs as the catalyst selectively promotes the dehydrogenation of the alcohol group to form the aldehyde.

Table 1 summarizes the performance of numerous Co_3O_4-based catalysts in the electrochemical reduction of carbon dioxide, highlighting the influence of catalyst morphology, composition, electrolyte, applied potential, and their impact on product selectivity, faradaic efficiency, and operational stability. The CO_2 electroreduction performance of various Co_3O_4-based catalysts was compared (Table 1). Co_3O_4/N-GO nano-cubes and atomic Co layers showed the highest formate (HCOOH) faradaic efficiencies (83% and 90%), while ultrathin Co_3O_4 had moderate formate selectivity (60%) with longer stability (20 h). Flower-like Co_3O_4 and Co_3O_4/P-rGO favored acetate (CH_3COOH) formation (69% and 58%), but with shorter stability (~2.5 h). Other morphologies promoted CO, ethanol, or ethylene production. This shows that morphology and support strongly affect selectivity, and nano-engineering strategies like rGO supports can enhance both product formation and stability. It can be observed that flower-like Co_3O_4/P-rGO achieves notable acetate production through synergistic effects of the support, despite moderate stability.

4. Conclusion

We have synthesized flower-like Co_3O_4 and demonstrated its potential as an efficient catalyst for the electrochemical conversion of CO_2 gas to ethanoic acid in aqueous bicarbonate medium, achieving a high faradaic efficiency of 69%. The catalytic activity was significantly enhanced by integrating flower-like Co_3O_4 with P-doped rGO, forming a hybrid catalyst that facilitated the selective production of ethanoic acid and propanal with 58% and 9% faradaic efficiencies, respectively. The hybrid system not only exhibits excellent product selectivity but also maintains robust electrochemical stability throughout the CO_2 reduction process. The synergistic interaction between Co_3O_4 and P-rGO likely promotes multi-electron transfer pathways, enabling the formation of complex molecules such as propanal. This work provides mechanistic insight into CO_2 electroreduction and opens a new avenue for producing renewable, value-added chemicals from greenhouse gas CO_2, and offers a promising strategy to address environmental and energy-related challenges.

Author contributions

Rad Mosharrof Mim: writing – review & editing, writing – original draft, methodology, investigation, formal analysis. Md. Shamim-Alam – writing – review & editing, Sangjukta Yesmin: writing – review & editing. Md. Mominul Islam: writing – review & editing, investigation, formal analysis. Chanchal Kumar Roy: writing – original draft, methodology, formal analysis. Abu Bin Imran: writing – review & editing, writing – original draft, methodology, investigation, formal analysis, conceptualization. Al-Nakib Chowdhury: writing – review & editing, writing – original draft, project administration, methodology, investigation, funding acquisition, formal analysis, conceptualization.

Conflicts of interest

There are no conflicts to declare.

Data availability

All data supporting the findings of this study are included within the manuscript and its supplementary information (SI).

No additional datasets were generated or analyzed. Supplementary information is available. See DOI: https://doi.org/10.1039/d6ra01555g.

Acknowledgements

The authors express their gratitude for the financial assistance provided by the Centre for Advanced Scientific Research (CASR), Bangladesh University of Engineering and Technology (BUET).

References

1 L. Ren, S. Zhou, T. Peng and X. Ou, A review of CO2 emissions reduction technologies and low-carbon development in the iron and steel industry focusing on China, *Renewable Sustainable Energy Rev.*, 2021, **143**, 110846, DOI: 10.1016/j.rser.2021.110846.

2 Q. Chen, P. Tsiakaras and P. Shen, Electrochemical Reduction of Carbon Dioxide: Recent Advances on Au-Based Nanocatalysts, *Catalysts*, 2022, **12**(11), 1348, DOI: 10.3390/catal12111348.

3 International Energy Agency, *Global Energy Review 2025: CO_2 Emissions*, IEA, Paris, 2025, available at: https://www.iea.org/reports/global-energy-review-2025.

4 J. Wang and W. Azam, Natural resource scarcity, fossil fuel energy consumption, and total greenhouse gas emissions in top emitting countries, *Geosci. Front.*, 2023, **15**, 101757, DOI: 10.1016/j.gsf.2023.101757.

5 A. Mustafa, B. G. Lougou, Y. Shuai, Z. Wang, S. Razzak, *et al.*, Recent progresses in the mechanism, performance, and fabrication methods of metal-derived nanomaterials for efficient electrochemical CO2 reduction, *J. Mater. Chem. A*, 2021, **9**(8), 4558–4588, DOI: 10.1039/D0TA11111B.

6 K. Deng, M. Du, W. Wang, F. Liu, D. Liang, F. Liu and D. Liang, Electrochemical CO2 reduction: From catalysts to reactive thermodynamics and kinetics, *Carbon Capture Sci. Technol.*, 2023, **6**, 100081, DOI: 10.1016/j.ccst.2022.100081.

7 D. Dedić, A. Dorniak, U. Rinner and W. Schöfberger, Recent Progress in (Photo-)Electrochemical Conversion of CO2 With Metal Porphyrinoid-Systems, *Front. Chem.*, 2021, **9**, 685619, DOI: 10.3389/fchem.2021.685619.

8 X.-Q. Wang, Q. Chen, Y.-J. Zhou, H.-M. Li, J.-w. Fu and M. Liu, Cu-based bimetallic catalysts for CO2 reduction reaction, *Adv. Sens. Energy Mater.*, 2022, **1**(3), 100023, DOI: 10.1016/j.asems.2022.100023.

9 A. H. Hatta, A. A. Jalil, N. S. Hassan, M. Y. S. Hamid, A. F. A. Rahman, L. P. Teh and D. Prasetyoko, A review on recent bimetallic catalyst development for synthetic natural gas production via CO methanation, *Int. J. Hydrogen Energy*, 2022, **47**(72), 30981–31002, DOI: 10.1016/j.ijhydene.2021.10.213.

10 F. Franco, C. Rettenmaier, H. S. Jeon and B. R. Cuenya, Transition metal-based catalysts for the electrochemical CO2 reduction: from atoms and molecules to nanostructured materials, *Chem. Soc. Rev.*, 2020, **49**(19), 6884–6946, DOI: 10.1039/D0CS00835D.

11 N. H. Khdary, A. S. Alayyar, L. M. Alsarhan, S. Alshihri and M. Mokhtar, Metal Oxides as Catalyst/Supporter for CO2 Capture and Conversion, Review, *Catalysts*, 2022, **12**(3), 300, DOI: 10.3390/catal12030300.

12 M. Asmare Tekalgne, H. H. Do, A. Hasani, Q. Van Le, H. W. Jang, S. H. Ahn and S. Y. Kim, Two-dimensional materials and metal-organic frameworks for the CO2 reduction reaction, *Mater. Today Adv.*, 2020, **5**, 100038, DOI: 10.1016/j.mtadv.2019.100038.

13 T. Van Phuc, S. G. Kang, J. S. Chung and S. H. Hur, Highly selective metal-organic framework-based electrocatalyst for the electrochemical reduction of CO2 to CO, *Mater. Res. Bull.*, 2021, **138**, 111228, DOI: 10.1016/j.materresbull.2021.111228.

14 A. Roy, H. S. Jadhav and J. Gil Seo, Cu2O/CuO Electrocatalyst for Electrochemical Reduction of Carbon Dioxide to Methanol, *Electroanalysis*, 2021, **33**(3), 705–712, DOI: 10.1002/elan.202060265.

15 R. Kas, R. Kortlever, A. Milbrat, M. T. M. Koper, G. Mul and J. Baltrusaitis, Electrochemical CO2 reduction on Cu2O-derived copper nanoparticles: controlling the catalytic selectivity of hydrocarbons, *Phys. Chem. Chem. Phys.*, 2014, **16**(24), 12194–12201, DOI: 10.1039/C4CP01520G.

16 L.-X. Liu, Y. Zhou, Y.-C. Chang, J.-R. Zhang, L.-P. Jiang, W. Zhu and Y. Lin, Tuning Sn3O4 for CO2 reduction to formate with ultra-high current density, *Nano Energy*, 2020, **77**, 105296, DOI: 10.1016/j.nanoen.2020.105296.

17 S. Ning, J. Wang, D. Xiang, S. Huang, W. Chen, S. Chen and X. Kang, Electrochemical reduction of SnO2 to Sn from the Bottom: In-Situ formation of SnO2/Sn heterostructure for highly efficient electrochemical reduction of carbon dioxide to formate, *J. Catal.*, 2021, **399**, 67–74, DOI: 10.1016/j.jcat.2021.04.028.

18 M. A. Rodriguez-Olguin, C. Flox, R. Ponce-Pérez, R. Lipin and F. Ruiz-Zepeda, Chlorine in NiO promotes electroreduction of CO2 to formate, *Appl. Mater. Today*, 2022, **28**, 101528, DOI: 10.1016/j.apmt.2022.101528.

19 H. Yang, Y. Zhou, K. Chen, X. Yu, F. Sun, M. Wang, Z. Cheng, J. Zhang and Q. J. Niu, Effects of PbO2/Pb3O4 ratio alteration for enhanced electrochemical advanced oxidation performance, *J. Solid State Chem.*, 2021, **301**, 122277, DOI: 10.1016/j.jssc.2021.122277.

20 Q. Zhang, J. Du, A. He, Z. Liu and C. Tao, Low overpotential electrochemical CO2 reduction to formate on Co3O4–CeO2/low graphitic carbon catalyst with oxygen vacancies, *J. Solid State Chem.*, 2019, **279**, 120946, DOI: 10.1016/j.jssc.2019.120946.

21 B. Zhang, J. Zhang, J. Shi, D. Tan, L. Liu, F. Zhang, C. Lu, Z. Su, X. Tan, X. Cheng, B. Han, L. Zheng and J. Zhang, Manganese acting as a high-performance heterogeneous electrocatalyst in carbon dioxide reduction, *Nat. Commun.*, 2019, **10**(1), 2980, DOI: 10.1038/s41467-019-10854-1.

22 K. Urbanek, K. Spilarewicz, J. Yu and W. Macyk, Photocatalytic reduction of CO2 at (SnO2, Fe3O4)/TiO2 composite, *Mater. Today Sustain.*, 2023, **22**, 100386, DOI: 10.1016/j.mtsust.2023.100386.

23 C. Yao, H. Fan, A. Adogwa, H. Xiong, M. Yang, F. Liu, Z. Chen and Y. Lou, Recent advances in carbon dioxide selective hydrogenation and biomass valorization *via* single-atom catalysts, *Resour. Chem. Mater.*, 2023, **2**(3), 189–207, DOI: 10.1016/j.recm.2023.05.003.

24 M. Zhu, S. Yu, R. Ge, L. Feng, Y. Yu, Y. Li and W. Li, Cobalt Oxide Supported on Phosphorus-Doped g-C3N4 as an Efficient Electrocatalyst for Oxygen Evolution Reaction, *ACS Appl. Energy Mater.*, 2019, **2**(7), 4718–4729, DOI: 10.1021/acsaem.9b00273.

25 A. Efremova, T. Rajkumar, Á. Szamosvölgyi, A. Sápi, K. Baán, I. Szenti, J. Gómez-Pérez, G. Varga, J. Kiss, G. Halasi, Á. Kukovecz and Z. Kónya, Complexity of a Co3O4 System under Ambient-Pressure CO2 Methanation: Influence of Bulk and Surface Properties on the Catalytic Performance, *J. Phys. Chem. C*, 2021, **125**(13), 7130–7141, DOI: 10.1021/acs.jpcc.0c09717.

26 Z. Zhang, X. Ke, B. Zhang, J. Deng, Y. Liu, W. Liu, H. Dai, F.-R. Chen and M. Sui, Facet-Dependent Cobalt Ion Distribution on the Co3O4 Nanocatalyst Surface, *J. Phys. Chem. Lett.*, 2020, **11**(22), 9913–9919, DOI: 10.1021/acs.jpclett.0c02901.

27 A. Aljabour, H. Coskun, D. Hazar Apaydin, F. Ozel, A. W. Hassel, P. Stadler, N. S. Sariciftci and M. Kus, Nanofibrous cobalt oxide for electrocatalysis of CO2 reduction to carbon monoxide and formate in an acetonitrile-water electrolyte solution, *Appl. Catal., B*, 2018, **229**, 163–170, DOI: 10.1016/j.apcatb.2018.02.017.

28 S. Saha, S. Maitra, M. Chattopadhyaya, A. Sarkar, S. Haque, S. Roy and K. Kargupta, Unveiling the Electrocatalytic Activity of Crystal Facet-Tailored Cobalt Oxide-rGO Heterostructure Toward Selective Reduction of CO2 to Ethanol, *ACS Appl. Nano Mater.*, 2022, **5**(8), 10369–10382, DOI: 10.1021/acsanm.2c01703.

29 J.-T. Ren, Y.-L. Zheng, K. Yuan, L. Zhou, K. Wu and Y.-W. Zhang, Self-templated synthesis of Co3O4 hierarchical nanosheets from a metal–organic framework for efficient visible-light photocatalytic CO2 reduction, *Nanoscale*, 2020, **12**(2), 755–762, DOI: 10.1039/C9NR08669B.

30 L. Wang, J. Wan, Y. Zhao, N. Yang and D. Wang, Hollow Multi-Shelled Structures of Co3O4 Dodecahedron with Unique Crystal Orientation for Enhanced Photocatalytic CO2 Reduction, *J. Am. Chem. Soc.*, 2019, **141**(6), 2238–2241, DOI: 10.1021/jacs.8b13528.

31 R. Ranjan, J. Tekawadia, R. Jain, N. B. Mhamane, T. Raja and C. S. Gopinath, Co3O4 for sustainable CO2 reduction and possible fine-tuning towards selective CO production, *Chem. Eng. J.*, 2023, **471**, 144459, DOI: 10.1016/j.cej.2023.144459.

32 K. Cysewska, M. K. Rybarczyk, G. Cempura, J. Karczewski, M. Łapiński, P. Jasinski and S. Molin, The Influence of the Electrodeposition Parameters on the Properties of Mn-Co-Based Nanofilms as Anode Materials for Alkaline Electrolysers, *Materials*, 2020, **13**(11), 2662, DOI: 10.3390/ma13112662.

33 J. Zhao, Y. Zou, X. Zou, T. Bai, Y. Liu, R. Gao, D. Wang and G.-D. Li, Self-template construction of hollow Co3O4 microspheres from porous ultrathin nanosheets and efficient noble metal-free water oxidation catalysts, *Nanoscale*, 2014, **6**(13), 7255–7262, DOI: 10.1039/C4NR00002A.

34 S. Delgado, M. d. C. Arévalo, E. Pastor and G. García, Electrochemical Reduction of Carbon Dioxide on Graphene-Based Catalysts, *Molecules*, 2021, **26**(3), 572, DOI: 10.3390/molecules26030572.

35 F. Hu, S. Tong, K. Lu, C.-M. Chen and F.-Y. Su, Reduced graphene oxide supported Ni-Ce catalysts for CO2 methanation: The support and ceria promotion effects, *J. CO_2 Util.*, 2019, **34**, 676–687, DOI: 10.1016/j.jcou.2019.08.020.

36 R. Aydin and F. Köleli, Electrochemical reduction of CO2 on a polyaniline electrode under ambient conditions and at high pressure in methanol, *J. Electroanal. Chem.*, 2002, **535**(1), 107–112, DOI: 10.1016/S0022-0728(02)01151-8.

37 G. W. Woyessa, J.-B. dela Cruz, M. Rameez and C.-H. Hung, Nanocomposite catalyst of graphitic carbon nitride and Cu/Fe mixed metal oxide for electrochemical CO2 reduction to CO, *Appl. Catal., B*, 2021, **291**, 120052, DOI: 10.1016/j.apcatb.2021.120052.

38 J. Liu, Y. Niu, X. He, J. Qi and X. Li, Photocatalytic Reduction of CO_2 Using TiO_2-Graphene Nanocomposites, *J. Nanomater.*, 2016, **2016**, e6012896, DOI: 10.1155/2016/6012896.

39 R. Damastuti, D. Susanti, A. Prasannan, W. Wei-Wen Hsiao and P.-D. Hong, High Selectivity Fuel from Efficient CO2 Conversion by Zn-Modified rGO and Amine-Functionalized CuO as a Photocatalyst, *Materials*, 2023, **16**(12), 4314, DOI: 10.3390/ma16124314.

40 Z. Moosapour Siahkalroudi, B. Aghabarari, M. Vaezi, E. Rodríguez-Castellón and M. Victoria Martínez-Huerta, Effect of secondary heteroatom (S, P) in N-doped reduced graphene oxide catalysts to oxygen reduction reaction, *Mol. Catal.*, 2021, **502**, 111372, DOI: 10.1016/j.mcat.2020.111372.

41 Y. L. F. Musico, N. Kakati, M. F. M. Labata, J. D. Ocon and P.-Y. A. Chuang, One-pot hydrothermal synthesis of heteroatom co-doped with fluorine on reduced graphene oxide for enhanced ORR activity and stability in alkaline media, *Mater. Chem. Phys.*, 2019, **236**, 121804, DOI: 10.1016/j.matchemphys.2019.121804.

42 H.-m. Wang, H.-x. Wang, Y. Chen, Y.-j. Liu, Z. Jing-xiang, Q.-h. Cai and X.-z. Wang, Phosphorus-doped graphene and (8, 0) carbon nanotube: Structural, electronic, magnetic properties, and chemical reactivity, *Appl. Surf. Sci.*, 2013, **273**, 302–309, DOI: 10.1016/j.apsusc.2013.02.035.

43 X. Yu, H. J. Kim, J.-Y. Hong, Y. M. Jung, K. D. Kwon and H. S. Park, Elucidating surface redox charge storage of phosphorus-incorporated graphenes with hierarchical architectures, *Nano Energy*, 2015, **15**, 576–586, DOI: 10.1016/j.nanoen.2015.05.010.

44 S. Some, I. Shackery, S. J. Kim and S. Chan Jun, Phosphorus-Doped Graphene Oxide Layer as a Highly Efficient Flame Retardant, *Chem.–Eur. J.*, 2015, **21**(44), 15480–15485, DOI: 10.1002/chem.201502170.

45 G. Bharath, K. Rambabu, C. Aubry, M. Abu Haija, A. Haija Nadda, N. Ponpandian and F. Banat, Self-Assembled Co3O4 Nanospheres on N-Doped Reduced Graphene Oxide (Co3O4/N-RGO) Bifunctional Electrocatalysts for Cathodic Reduction of CO2 and Anodic Oxidation of Organic Pollutants, *ACS Appl. Energy Mater.*, 2021, **4**(10), 11408–11418, DOI: 10.1021/acsaem.1c02196.

46 X. Chen, Z. Qu, Z. Liu and G. Ren, Mechanism of Oxidization of Graphite to Graphene Oxide by the Hummers Method, *ACS Omega*, 2022, **7**(27), 23503–23510, DOI: 10.1021/acsomega.2c01963.

47 W. Lv, R. Zhang, P. Gao and L. Lei, Studies on the faradaic efficiency for electrochemical reduction of carbon dioxide to formate on tin electrode, *J. Power Sources*, 2014, **253**, 276–281, DOI: 10.1016/j.jpowsour.2013.12.063.

48 F. Wah Low, C. W. Lai and S. B. A. Hamid, Easy preparation of ultrathin reduced graphene oxide sheets at a high stirring speed, *Ceram. Int.*, 2015, **41**(4), 5798–5806, DOI: 10.1016/j.ceramint.2015.01.008.

49 N. M. S. Hidayah, W.-W. Liu, C.-W. Lai, N. Z. Noriman, C.-S. Khe, U. Hashim and H. Cheun Lee, Comparison on graphite, graphene oxide and reduced graphene oxide: Synthesis and characterization, *AIP Conf. Proc.*, 2017, **1892**(1), 150002, DOI: 10.1063/1.5005764.

50 H. Maharana, P. K. Rai and A. Basu, Surface-mechanical and electrical properties of pulse electrodeposited Cu–graphene oxide composite coating for electrical contacts, *J. Mater. Sci.*, 2017, **52**(2), 1089–1105, DOI: 10.1007/s10853-016-0405-7.

51 W. Cao, W. Wang, H. Shi, J. Wang, M. Cao, Y. Liang and M. Zhu, Hierarchical three-dimensional flower-like Co3O4 architectures with a mesocrystal structure as high capacity anode materials for long-lived lithium-ion batteries, *Nano Res.*, 2018, **11**(3), 1437–1446, DOI: 10.1007/s12274-017-1759-0.

52 P. Cui, J. Lee, E. Hwang and H. Lee, One-pot reduction of graphene oxide at subzero temperatures, *Chem. Commun.*, 2011, **47**(45), 12370, DOI: 10.1039/c1cc15569e.

53 S. Chakrabarty, R. M. Mim, N. T. Tonu, M. H. Ara and P. K. Dhar, Removal of Toxic Pb (II) Ion from Aqueous Solution Using ZnO/K2SO4 Nanocomposites: Kinetics, Isotherms and Error Function Analyses, *Chem. Afr.*, 2024, **7**(3), 1467–1480, DOI: 10.1007/s42250-023-00843-9.

54 X. Wang, H. Zhao, L. Chang, Z. Yu, Z. Xiao, S. Tang, C. Huang, J. Fan and S. Yang, First-Principles Study on Interlayer Spacing and Structure Stability of NiAl-Layered Double Hydroxides, *ACS Omega*, 2022, **7**(43), 39169–39180, DOI: 10.1021/acsomega.2c05067.

55 X. Zhu, G. Ning, X. Ma, Z. Fan, C. Xu, J. Gao, C. Xu and F. Wei, High density Co3O4 nanoparticles confined in a porous graphene nanomesh network driven by an electrochemical process: ultra-high capacity and rate performance for lithium ion batteries, *J. Mater. Chem. A*, 2013, **1**(44), 14023, DOI: 10.1039/c3ta12824e.

56 L. Dai, M. Liu, Y. Song, J. Liu and F. Wang, Mn3O4-decorated Co3O4 nanoparticles supported on graphene oxide: Dual electrocatalyst system for oxygen reduction reaction in alkaline medium, *Nano Energy*, 2016, **27**, 185–195, DOI: 10.1016/j.nanoen.2016.07.007.

57 S. Mourdikoudis, R. M. Pallares and N. T. K. Thanh, Characterization techniques for nanoparticles: comparison and complementarity upon studying nanoparticle properties, *Nanoscale*, 2018, **10**(27), 12871–12934, DOI: 10.1039/c8nr02278j.

58 V. Georgalikas, J. N. Tiwari, C. Kemp, J. A. Perman, A. B. Bourlinos, K. S. Kim and R. Zbroil, Noncovalent Functionalization of Graphene and Graphene Oxide for Energy Materials, Biosensing, Catalytic, and Biomedical Applications, *Chem. Rev.*, 2016, **116**(9), 5465–5519, DOI: 10.1021/acs.chemrev.5b00620.

59 J. Wu, X. Zheng, C. Jin, J. Tian and R. Yang, Ternary doping of phosphorus, nitrogen, and sulfur into porous carbon for enhancing electrocatalytic oxygen reduction, *Carbon*, 2015, **92**, 327–338, DOI: 10.1016/j.carbon.2015.05.013.

60 J. Peter Paraknowitsch and A. Thomas, Doping carbons beyond nitrogen: an overview of advanced heteroatom doped carbons with boron, sulphur and phosphorus for energy applications, *Energy Environ. Sci.*, 2013, **6**(10), 2839, DOI: 10.1039/c3ee41444b.

61 E. Pervaiz, M. S. A. Virk, Z. Bingxue, C. Yin and M. Yang, Nitrogen doped RGO–Co3O4 nanograin cookies: highly porous and robust catalyst for removing nitrophenol from waste water, *Nanotechnology*, 2017, **28**(38), 385703, DOI: 10.1088/1361-6528/aa8297.

62 H. Inta, M. Koppisetti, S. Ganguli and V. Mahalingam, Electrochemical Reconstruction of Zn 0.3 Co 2.7 (PO 4) 2 ·4H 2 O for Enhanced Water Oxidation Performance, *ACS Appl. Energy Mater.*, 2020, **3**, 12088–12098, DOI: 10.1021/acsaem.0c02200.

63 Y. Xue, X. Zuo, Y. Li, H. Liu and Y. Li, Graphdiyne-Supported $NiCo_2S_4$ Nanowires: A Highly Active and Stable 3D Bifunctional Electrode Material, *Small*, 2017, **13**(31), 1700936, DOI: 10.1002/smll.201700936.

64 E. Pervaiz, M. S. A. Virk, Z. Bingxue, C. Yin and M. Yang, Nitrogen doped RGO–Co_3O_4 nanograin cookies: highly porous and robust catalyst for removing nitrophenol from waste water, *Nanotechnology*, 2017, **28**(38), 385703, DOI: 10.1088/1361-6528/aa8297.

65 Z.-Z. Ma, Y.-S. Wang, B. Liu, H. Jiao and L. Xu, A Non–Enzymatic Electrochemical Sensor of Cu@Co–MOF Composite for Glucose Detection with High Sensitivity and Selectivity, *Chemisensors*, 2022, **10**, 10, DOI: 10.3390/chemosensors10100416.

66 M. Rahaman, M. F. Islam, Z. M. Moushumy, M. M. Hossain, M. Nurnobi Islam, M. Hasan, M. A. Rahman, N. A. Tanjila and M. A. Hasnat, Electrokinetics of CO2 Reduction in Imidazole Medium Using RuO2.SnO2-Immobilized Glassy Carbon Electrode, *Molecules*, 2025, **30**(3), 575, DOI: 10.3390/molecules30030575.

67 O. Van Der Heijden, S. Park, R. E. Vos, J. J. J. Eggebeen and M. T. M. Koper, Tafel Slope Plot as a Tool to Analyze Electrocatalytic Reactions, *ACS Energy Lett.*, 2024, **9**(4), 1871–1879, DOI: 10.1021/acsenergylett.4c00266.

68 Z. Sun, T. Ma, H. Tao, Q. Fan and B. Han, Fundamentals and Challenges of Electrochemical CO2 Reduction Using Two-Dimensional Materials, *Chem*, 2017, **3**(4), 560–587, DOI: 10.1016/j.chempr.2017.09.009.

69 F. Ju, J. Zhang and W. Lu, Efficient Electrochemical Reduction of CO2 to CO in Ionic Liquid/Propylene Carbonate Electrolyte on Ag Elect, *Catalysts*, 2020, **10**(10), 1102, DOI: 10.3390/catal10101102.

70 C. Sandford, M. A. Edwards, K. J. Klunder, D. P. Hickey, M. Li, K. Barman, M. S. Sigman, H. S. White and S. D. Minteer, A synthetic chemist's guide to electroanalytical tools for studying reaction mechanisms, *Chem. Sci.*, 2019, **10**(26), 6404–6422, DOI: 10.1039/C9SC01545K.

71 E. Bertheussen, Y. Abghoui, Z. P. Jovanov, A.-S. Varela, I. E. L. Stephens and I. Chorkendorff, Quantification of liquid products from the electroreduction of CO2 and CO using static headspace-gas chromatography and nuclear magnetic resonance spectroscopy, *Catal. Today*, 2017, **288**, 54–62, DOI: 10.1016/j.cattod.2017.02.029.

72 M. Berholts, H. Myllynen, K. Kooser, E. Itälä, S. Granroth, H. Levola, J. K. Laksman, S. Oghbaiee, B. Oostenrijk, E. Nõmmiste and E. Kukk, Photofragmentation of gas-phase acetic acid and acetamide clusters in the vacuum ultraviolet region, *J. Chem. Phys.*, 2017, **147**(19), 194302, DOI: 10.1063/1.4999686.

73 R. De, S. Gonglach, S. Paul, M. Haas, S. S. Sreejith, P. Gerschel, U.-P. Apfel, T. Huyen Vuong, J. Rabeah, S. Roy and W. Schöfberger, Electrocatalytic Reduction of CO2 to Acetic Acid by a Molecular Manganese Corrole Complex, *Angew. Chem., Int. Ed.*, 2020, **59**(26), 10527–10534, DOI: 10.1002/anie.202000601.

74 Z. Sun, T. Ma, H. Tao, Q. Fan and B. Han, Fundamentals and Challenges of Electrochemical CO2 Reduction Using Two-Dimensional Materials, *Chem*, 2017, **3**(4), 560–587, DOI: 10.1016/j.chempr.2017.09.009.

75 T. Liu, J. Sang, H. Li, P. Wei, Y. Zang and G. Wang, Towards understanding of CO2 electroreduction to C2+ products on copper-based catalysts, *Battery Energy*, 2022, **1**(4), 20220012, DOI: 10.1002/bte2.20220012.

76 C. Genovese, C. Ampelli, S. Perathoner and G. Centi, Mechanism of C-C bond formation in the electrocatalytic reduction of CO2 to acetic acid. A challenging reaction to use renewable energy with chemistry, *Green Chem.*, 2017, **19**, 2406–2415, DOI: 10.1039/C6GC03422E.

77 V. Kumaravel, J. Bartlett and S. C. Pillei, Photoelectrochemical Conversion of Carbon Dioxide (CO2) into Fuels and Value-Added Products, *ACS Energy Lett.*, 2020, **5**, 486–519, DOI: 10.1021/acsenergylett.9b02585.

78 N. Sakamoto, K. Sekizawa, S. Shirai, T. Nonaka, T. Arai and S. Sato, Dinuclear Cu(I) molecular electrocatalyst for CO2-to-C3 product conversion, *Nat. Catal.*, 2024, **7**, 574–584, DOI: 10.1038/s41929-024-01147-y.

79 L. Rotundo, S. Ahmad, C. Cappuccino, A. J. Pearce, H. Nedzbala, S. R. Bottum, J. M. Mayer, J. F. Cahoon, C. Grills, M. Z. Ertem and G. F. Manbeck, Fast Catalysis at Low Overpotential: Designing Efficient Dicationic Re(bpy2+) (CO)3I Electrocatalysts for CO2 Reduction, *J. Am. Chem. Soc.*, 2024, **146**(36), 24742–24747, DOI: 10.1021/jacs.4c08084.

80 X. Tan and J. Nielsen, The integration of bio-catalysis and electrocatalysis to produce fuels and chemicals from carbon dioxide, *Chem. Soc. Rev.*, 2022, **51**(11), 4763–4785, DOI: 10.1039/D2CS00309K.

81 D. R. Weinberg, C. J. Gagliardi, J. F. Hull, C. F. Murphy, C. A. Kent, B. Westlake, A. Paul, D. H. Ess, D. Granville McCafferty and T. J. Meyer, Proton-Coupled Electron Transfer, *Chem. Rev.*, 2007, **107**(11), 5004–5064, DOI: 10.1021/cr0500030.

82 A. P. Markusse, B. F. M. Kuster and J. C. Schouten, Platinum catalysed aqueous alcohol oxidation: experimental studies and reaction model discrimination, *J. Mol. Catal. A: Chem.*, 2000, **158**(1), 215–222, DOI: 10.1016/S1381-1169(00)00082-0.

83 W. Chen, B. Han, T. Chen, X. Liu, S. Liang, H. Deng and Z. Lin, MOFs-derived ultrathin holey Co3O4 nanosheets for enhanced visible light CO2 reduction, *Appl. Catal., B*, 2019, **244**, 996–1003, DOI: 10.1016/j.apcatb.2018.12.045.

84 P. Sekar, L. Calvillo, C. Tubaro, M. Baron, A. Pokle, F. Carraro and S. Agnoli, Cobalt Spinel Nanocubes on N-Doped Graphene: A Synergistic Hybrid Electrocatalyst for the Highly Selective Reduction of Carbon Dioxide to Formic Acid, *ACS Catal.*, 2017, **7**(11), 7695–7703, DOI: 10.1021/acscatal.7b02166.

85 Y. Wang, T. Zheng, Y. Jin, T. Sun, X. Ding and X. Wang, Multiscale structural engineering of cobalt single-atom catalyst for highly efficient photocatalytic CO2 reduction, *Sci. China Mater.*, 2024, **67**(4), 1292–1300, DOI: 10.1007/s40843-023-2793-3.

86 S. Gao, Z. Sun, W. Liu, X. Jiao, X. Zu, Q. Hu, Y. Sun, T. Yao, W. Zhang, S. Wei and Y. Xie, Atomic layer confined vacancies for atomic-level insights into carbon dioxide electroreduction, *Nat. Commun.*, 2017, **8**(1), 14503, DOI: 10.1038/ncomms14503.

87 B. Matteo, S. Rej, A. Naldoni, T. Montini, M. Bevilacqua and P. Fornasiero, CO2 Electroreduction by Engineering the Cu2O/RGO Interphase, *Catalysts*, 2024, **14**(7), 24, DOI: 10.3390/catal14070412.

88 M. Isabel Cerrillo, C. Jiménez, M. Á. Ortiz, R. Camarillo, C. Rincón and F. Martínez, Electrocatalytic reduction of CO2 with N/B co-doped reduced graphene oxide-based catalysts, *J. Ind. Eng. Chem.*, 2023, **127**, 101–109, DOI: 10.1016/j.jiec.2023.06.039.